Atmos. Meas. Tech. Discuss., 8, 3883–3932, 2015
www.atmos-meas-tech-discuss.net/8/3883/2015/
doi:10.5194/amtd-8-3883-2015

Atmospheric Measurement Techniques Discussions

HO_x radical chemistry in oxidation flow reactors with low-pressure mercury lamps systematically examined by modeling

Z. Peng[1,2], D. A. Day[1,2], H. Stark[1,2,3], R. Li[1,4,5], B. B. Palm[1,2], W. H. Brune[6], and J. L. Jimenez[1,2]

[1]Cooperative Institute for Research in Environmental Sciences, University of Colorado, Boulder, CO 80309, USA
[2]Department of Chemistry and Biochemistry, University of Colorado, Boulder, CO 80309, USA
[3]Aerodyne Research, Inc., Billerica, MA 01821, USA
[4]Department of Atmospheric and Oceanic Sciences, University of Colorado, Boulder, CO 80309, USA
[5]Chemical Sciences Division, Earth System Research Laboratory, National Oceanic and Atmospheric Administration, Boulder, CO 80305, USA
[6]Department of Meteorology, Pennsylvania State University, University Park, PA 16802, USA

Received: 4 March 2015 – Accepted: 31 March 2015 – Published: 20 April 2015

Correspondence to: J. L. Jimenez (jose.jimenez@colorado.edu)

Published by Copernicus Publications on behalf of the European Geosciences Union.

Abstract

Oxidation flow reactors (OFRs) using OH produced from low-pressure Hg lamps at 254 nm (OFR254) or both 185 and 254 nm (OFR185) are commonly used in atmospheric chemistry and other fields. OFR254 requires the addition of externally formed O_3 since OH is formed from O_3 photolysis, while OFR185 does not since O_2 can be photolyzed to produce O_3 and OH can also be formed from H_2O photolysis. In this study, we use a plug-flow kinetic model to investigate OFR properties under a very wide range of conditions applicable to both field and laboratory studies. We show that the radical chemistry in OFRs can be characterized as a function of UV light intensity, H_2O concentration, and total external OH reactivity (OHR_{ext}, e.g., from VOCs, NO_x, and SO_2). OH exposure is decreased by added external OH reactivity. OFR185 is especially sensitive to this effect at low UV intensity due to low primary OH production. OFR254 can be more resilient against OH suppression at high injected O_3 (e.g., 70 ppm), as a larger primary OH source from O_3, as well as enhanced recycling of HO_2 to OH, make external perturbations to the radical chemistry less significant. However if the external OH reactivity in OFR254 is much larger than OH reactivity from injected O_3, OH suppression can reach two orders of magnitude. For a typical input of 7 ppm O_3 ($OHR_{O_3} = 10\,s^{-1}$) ten-fold OH suppression is observed at $OHR_{ext} \sim 100\,s^{-1}$, which is similar or lower than used in many laboratory studies. This finding may have important implications for the interpretation of past laboratory studies, as applying OH_{exp} measurements acquired under different conditions could lead to over an order-of-magnitude error in the estimated OH_{exp}. The uncertainties of key model outputs due to uncertainty in all rate constants and absorption cross-sections in the model are within ±25 % for OH exposure and within ±60 % for other parameters. These uncertainties are small relative to the dynamic range of outputs. Uncertainty analysis shows that most of the uncertainty is contributed by photolysis rates of O_3, O_2, and H_2O and reactions of OH and HO_2 with themselves or with some abundant species, i.e., O_3 and H_2O_2. Using HO_x-recycling vs. destructive external OH reactivity only leads to small changes in

AMTD
8, 3883–3932, 2015

OH_{exp} under most conditions. Changing the identity (rate constant) of external OH reactants can result in substantial changes in OH_{exp} due to different reductions in OH suppression as the reactant is consumed. We also report two equations for estimating OH exposure in OFR254. We find that the equation estimating OH_{exp} from measured O_3 consumption performs better than an alternative equation that does not use it, and thus recommend measuring both input and output O_3 concentrations in OFR254 experiments. This study contributes to establishing a firm and systematic understanding of the gas-phase HO_x and O_x chemistry in these reactors, and enables better experiment planning and interpretation as well as improved design of future reactors.

1 Introduction

Species emitted into the Earth's atmosphere are degraded by oxidative chemistry dominated by the OH radical. OH oxidation plays an important role in self-cleaning of the atmosphere (Levy II, 1971), O_3 production, and formation of secondary aerosols (Volkamer et al., 2006; Hallquist et al., 2009).

Because of the very low ambient concentrations of the atmospheric oxidants, oxidation timescales in the atmosphere can be long. They range from several hours (e.g., isoprene) to months (e.g., acetone) or longer (e.g., CH_4), which presents challenges for studying this chemistry directly in the atmosphere as other processes such as advection, deposition, mixing etc. happen in parallel. Atmospheric simulation chambers using UV light sources above 300 nm (e.g., UV blacklights or Xe arclamps, or outdoor solar radiation) have been used for many decades to study atmospheric oxidation processes in a manner that decouples them from transport and other processes (Cocker et al., 2001; Carter et al., 2005; Presto et al., 2005; Wang et al., 2011; Platt et al., 2013). However such chambers have some shortcomings such as long simulation times of hours, inability to reach high OH exposures as needed to fully simulate long atmospheric residence times, significant wall loss of gases and particles, and difficulty in performing experiments with ambient air (George et al., 2007; Kang et al., 2007; Carl-

AMTD
8, 3883–3932, 2015

ton et al., 2009; Seakins, 2010; Wang et al., 2011). An alternative type of reactor has been developed to overcome those limitations using lamps producing wavelengths not present in the troposphere to produce high oxidant concentrations, while allowing ambient air to flow through the reactor. For example oxidation flow reactors (OFRs) using low-pressure Hg lamps can produce OH in large concentrations from H_2O and/or O_3 photolysis, enabling short residence times and hence reduce wall losses. In addition to use in reactors for atmospheric studies, chemistry initiated with low-pressure Hg lamps is also widely used in other fields, e.g., water and air purification (Legrini et al., 1993; Andreozzi et al., 1999; Johnson et al., 2014; Ye et al., 2014), chemical analysis (Danet et al., 2009; Ma and Xia, 2014), photochemical vapor deposition (Kumata et al., 1986), and optical pumping for laser generation (Witte et al., 1979).

The UV light used in OFRs is typically either at 254 nm ("OFR254") or both 185 and 254 nm ("OFR185"). OFR254 requires the addition of externally formed O_3 since OH is formed only via O_3 photolysis at 254 nm. OFR185 does not require this addition since OH can be formed from H_2O photolysis at 185 nm. O_3 is also formed in OFR185 from O_2 photolysis at 185 nm. Because of their short experimental time scales and ease of use in the field, OFRs have gained popularity in both field and laboratory studies, in particular for research on secondary organic aerosols (SOA) (Massoli et al., 2010; Cubison et al., 2011; Kang et al., 2011; Lambe et al., 2011a, b, 2012, 2013; Bahreini et al., 2012; Saukko et al., 2012; Wang et al., 2012; Li et al., 2013; Ortega et al., 2013; Tkacik et al., 2014). These studies were conducted under a wide range of experimental conditions, e.g., relative humidity, UV light intensity, and VOC and NO_x concentrations.

In spite of the wide application of the radical chemistry in OFRs, the quantitative characterization of the radical chemistry itself has been extremely limited. To study the radical chemistry in OFRs experimentally, measurements of radicals over a very wide range of conditions would be needed, which are difficult and expensive to conduct. Modeling studies thus offer a very useful strategy for the characterization of OFR gas-phase radical chemistry. Although individual radical reactions relevant to OFRs with low-pressure Hg lamps are well known (Sander et al., 2011), to our knowledge,

AMTD
8, 3883–3932, 2015

only two such modeling studies have been performed to date for OFR185 (Ono et al., 2014; Li et al., 2015), and none for OFR254. Ono et al. (2014) investigated the dependence of the consumption of O_3 and some radicals on H_2O concentration (abbr. H_2O hereinafter) in OFR185 with their model. The kinetic model that Li et al. (2015) developed compared well against measurements of OH exposure (OH_{exp}) and O_3 concentration (abbr. O_3 hereinafter) in laboratory calibration experiments and field studies using OFR185. They showed that OH exposure (OH_{exp}) in OFR185 increases strongly with UV light intensity (abbr. UV hereinafter), H_2O, and residence time, and decreases strongly with external OH reactivity (OHR_{ext}, i.e., the inverse of the OH lifetime against loss to external reactants, calculated as the sum of the products of concentrations of externally introduced OH-consuming species and rate constants of their reactions with OH). However these authors did not report any results for OFR254, nor did they quantify the parametric uncertainties in their models, consider cases with very high OHR_{ext} that have been used in multiple published experiments, or consider different types of OHR_{ext}.

In this paper, we use an improved version of the Li et al. (2015) model to systematically characterize the radical chemistry in OFRs as a function of the three main parameters: UV, H_2O, and OHR_{ext}. These are the parameters upon which OH exposure in OFR185 has been shown to mainly depend (Li et al., 2015), and thus, we investigate a very large space spanned by these parameters, rather than choosing a few discrete points. We also study the effects of some additional parameters regulating the radical chemistry, i.e., extent of HO_x destruction vs. recycling by OHR_{ext}, the identity of the external OH reactants, and the amount of initially injected O_3 in OFR254. In addition, the uncertainties of kinetic parameters are considered in this study and the corresponding output uncertainties, as well as the contribution of key parameters to those uncertainties, are estimated by Monte Carlo uncertainty propagation. This study provides credible answers to key uncertainties about the chemistry in OFRs, thus enabling better experimental interpretation and design for future studies.

AMTD
8, 3883–3932, 2015

2 Methods

In this section, we briefly introduce the OFR we use (Sect. 2.1), and then describe the model and the experimental conditions for OFRs in this study (Sect. 2.2). The method for uncertainty and sensitivity analysis is presented in Sect. 2.3.

2.1 Potential Aerosol Mass flow reactor

Kang et al. (2007) introduced the Potential Aerosol Mass (PAM) flow reactor, an OFR designed for secondary aerosol formation studies. This type of OFR has been used by multiple groups, in particular to study SOA formation and aging (Massoli et al., 2010; Cubison et al., 2011; Kang et al., 2011; Lambe et al., 2011a, b, 2012, 2013; Bahreini et al., 2012; Saukko et al., 2012; Wang et al., 2012; Li et al., 2013; Ortega et al., 2013). Although earlier versions had different geometry, the version of the PAM reactor used in almost all publications and currently in use by all groups is a cylindrical vessel with an approximate volume of 13 L. Some versions are made completely of coated aluminum, while others are part aluminum and part glass. Low-pressure Hg UV lamps (model no. 82-9304-03, BHK Inc.) are installed inside the reactor to produce UV light at 185 and 254 nm. Experiments using 1, 2, and 4 lamps have been reported. The UV intensity can be rapidly changed via the Hg lamp voltages. The OFR185 mode uses Teflon sleeves for the lights, which transmits both wavelengths (Li et al., 2015), which allows ambient or sample air alone to be processed by the reactor. If quartz sleeves are used, the 185 nm light is removed, leaving photons at 254 nm for the photochemical generation of OH radicals (OFR254 mode). In that case, externally generated O_3 is introduced into the reactor, along with the ambient/sample air. As discussed below, the chemistry in OFR254 mode is strongly dependent on the amount of injected O_3. For this reason we will adopt the nomenclature OFR254-X where X is the injected O_3 concentration in ppm, e.g. OFR254-70 and OFR254-7 starting with 70 and 7 ppm O_3, respectively.

AMTD
8, 3883–3932, 2015

2.2 Model description

The model used in the present study is based on that of Li et al. (2015). It is a standard chemical-kinetic plug flow model. Li et al.'s model includes all O_x and HO_x photolysis and thermal reactions whose kinetic data are available in the JPL Chemical Kinetic Data Evaluation (Sander et al., 2011) and several reactions involving external OH reactivity (e.g., from SO_2, CO and NO_x, see Table 1 of Li et al., 2015). We implement this reaction scheme in the KinSim chemical kinetic integrator (http://www.igorexchange.com/node/1333) implemented in Igor Pro 6 (Wavemetrics, Lake Oswego, OR, USA). The stiff coupled system of ordinary differential equations is solved by the method of backward differentiation formula without any steady-state approximations using double precision variables. The integrator adaptively computes integration time steps that satisfy the mean square root of absolute error being lower than a threshold. To minimize the calculation time without diminishing the quality of the output concentrations, we set this threshold to 800 molecules cm^{-3}, which is orders of magnitude smaller than the concentrations of all species in this model, except $O(^1D)$. Furthermore, the $O(^1D)$ concentration should be highly accurate, since it is controlled by extremely fast reactions with the most abundant species (e.g, O_2, N_2, and O_3) with negligible *relative* error (the absolute error threshold of 800 molecules cm^{-3} for those species' concentrations ($> 10^{15}$ molecules cm^{-3}) results in negligible relative error, so that relative errors propagated into $O(^1D)$ concentration are also negligible). Compared to Li et al.'s model, this implementation in the KinSim integrator reduces the calculation time by a factor greater than 1000, allowing the exploration of the chemistry in a very large parameter (physical input conditions or kinetic parameters) space. The results of our independent implementation were found to be in agreement with those from the model of Li et al. (2015) within better than 1 % for all chemical species over a wide range of physical conditions.

In this study, we assume plug flow with a residence time of 180 s. Temperature and atmospheric pressure are set to 295 K and 835 mbar, respectively, which are typical

AMTD
8, 3883–3932, 2015

values in Boulder, CO, USA. The range of H_2O mixing ratios studied is 0.07–2.3 % (equivalent to a relative humidity range of 3–90 % at 295 K). We study four levels of external OH reactivity (OHR_{ext}) representing the range in most field and laboratory studies: 0, 10, 100, and 1000 s^{-1} (10 s^{-1} is equivalent to ~ 4 ppb isoprene, ~ 8 ppb α-pinene, ~ 70 ppb toluene, or ~ 30 ppb *n*-dodecane). SO_2 is used as the surrogate of external OH reactivity. In a recent study, Nehr et al. (2014) measured OHR vs. time in a few VOC reactions and in some it decreased with time and in others it increased and later decreased because of the continuing reactivity of the products. Therefore, although SO_2 is consumed by OH much more slowly than most primary VOCs, it is actually more realistic in terms of the decrease of total OH reactivity than using only the first generation reaction of a VOC, since the latter ignores the continuing reactivity of the products. Also importantly SO_2 + OH results in the production of HO_2 and thus is HO_x neutral. This is also applicable to reactions of OH with CO and (to a good approximation) VOCs, while OH + NO_2 does lead to HO_x destruction. The impact of HO_x conserving vs. destroying reaction and of the reaction rate of the OH reactant is investigated below. NO is quickly converted to NO_2 by the high levels of O_3 present, and NO_2 quickly forms HNO_3 by reaction with OH (Li et al., 2015). In the base case, SO_2 concentration decreases as it is consumed by OH in this study. In some additional cases, we also keep a constant OHR_{ext} or model different OHR_{ext} variations as surrogates of VOC oxidation (Fig. S1). For OFR254, we add 70 ppm externally formed O_3 (OFR254-70), as used in OFR254 experiments during the BEACHON-RoMBAS campaign (Palm et al., 2015), and also explore the chemistry when 7 ppm O_3 is added instead (OFR254-7), as has been done in other studies (Kang et al., 2011; Liu et al., 2015). The range of photon fluxes studied at 185 and 254 nm are 10^{11}–10^{14} and 4.2×10^{13}–8.5×10^{15} photons cm^{-2} s^{-1}, respectively, based on the characterization of Li et al. (2015). Within the ranges of the parameters explored, we also define several typical cases, which are labeled by two characters for low (L), medium (M), or high (H) H_2O and UV, respectively, and one character for 0, low (L), high (H), or very high (V) OHR_{ext} (Table 1).

AMTD
8, 3883–3932, 2015

2.3 Sensitivity and uncertainty analyses

It is of interest to characterize the degree of uncertainty of the outputs due to uncertain kinetic parameters, as well as the contributions of different parameters to the uncertainties of key outputs. For this analysis it is necessary to appropriately represent uncertain input kinetic parameters and propagate their uncertainties through the model. Note that because of the model's limitations, we do not assess the impact of some factors or input parameters that may lead to uncertain outputs, e.g., Hg lamp emission variations in space and time, variable UV fluxes at different points in the reactor, the assumption of plug flow, and the fact that temperature may vary by a few degrees due to incomplete removal of the lamp heat by the N_2 sheath flow. The effect of those parameters should be the focus of future studies.

2.3.1 Representation of uncertain kinetic parameters

To take parametric uncertainties into account, we use the formalism of the JPL Chemical Kinetic Data Evaluation (Sander et al., 2011). All uncertain rate constants and photoabsorption cross-sections (or partial cross-sections for multichannel photolysis) are assumed to have log-normal distributions, which ensure the positivity of these parameters and are commonly used to represent uncertainties in kinetic models (Hanna et al., 2001). The uncertainty factor f can be used as a measure of uncertainties of log-normally distributed random variables. It is defined as

$$f = e^{\sigma}, \tag{1}$$

where σ is the SD of the random variable's logarithm. Numerically, a random variable's uncertainty factor is approximately equal to 1 plus its relative uncertainty if the uncertainty is relatively small. In the JPL database, uncertainty factors of rate constants are given only at 298 K. To estimate the corresponding uncertainty factors at 295 K, we

AMTD
8, 3883–3932, 2015

apply the following formula recommended in the JPL data evaluation:

$$f(T) = f(298\,\mathrm{K}) \exp\left|g\left(\frac{1}{T} - \frac{1}{298\,\mathrm{K}}\right)\right|, \quad (2)$$

where T is temperature (in K), and g is a constant that parameterizes the additional uncertainty arising from the temperature effect (in K). Uncertainty factors of a few (partial) absorption cross sections used in the present model are not available in the JPL database. We thus use the uncertainties recommended for these cross sections by Hébrard et al. (2006).

2.3.2 Monte Carlo uncertainty propagation

To propagate the parametric uncertainty into the model outputs, BIPM et al. (2008) recommend sample-based Monte Carlo uncertainty propagation (MCUP) methods. By MCUP, we propagate representative samples of the input distributions to obtain output distributions, from which we compute all necessary statistics. To perform MCUP in the present model, an appropriate sampling of all rate constants and cross-sections is necessary. Considering their log-normality, we generate the random samples by the following method (Peng et al., 2012):

$$\ln k_{ij} = \ln k_i^0 + \epsilon_j \ln f_i, \quad (3a)$$

$$\ln \sigma_{mn} = \ln \sigma_m^0 + \epsilon_n \ln f_m, \quad (3b)$$

where k_i^0, f_i, and k_{ij} are the nominal value, the uncertainty factor, and the jth sample of the ith rate constant, respectively. ϵ_j is the jth sample of a random variable following the standard normal distribution. The (partial) cross-section samples, σ_{mn}, can be generated in the same way.

AMTD
8, 3883–3932, 2015

2.3.3 Correlation-based parametric uncertainty analysis

Li et al. (2015) performed a study of the sensitivity of four key model outputs, i.e., OH_{exp}, average O_3 and H_2O_2 concentrations, and HO_2/OH ratio, to model inputs of UV flux, pressure, temperature, residence time, H_2O, and OHR_{ext}. In the present work, we perform a complementary parametric uncertainty study that investigates the dependences of the same outputs, but on rate constants and absorption cross-sections. With the output from the Monte Carlo procedure from the previous section, we are able to calculate, at low computational expense, the relative contributions of the uncertain input parameters to the total output uncertainties.

The calculation of these relative contributions is a standard goal of uncertainty analysis (Saltelli et al., 2005). These contributions result from the amplification or reduction of the parameter uncertainties via the model during the propagation. Therefore, the contribution of a certain input parameter to the uncertainty of a given output depends on both the uncertainty on the parameter and the sensitivity of specific output to that input parameter (Saltelli et al., 2005; Wakelam et al., 2010).

To perform such an uncertainty analysis, we use a correlation-based method: we calculate the Spearman correlation coefficients between all model parameters and each of the four above-mentioned outputs, which is recommended for complex models (Wakelam et al., 2010). If higher-order effects are negligible, then the squared correlation coefficient between a model parameter and an output is equal to the corresponding parameter's relative contribution to the output (relative) variance (Saltelli et al., 2005). This method has been successfully applied to identify the reactions that have the most overall influence on the outputs in complex reaction networks (Peng et al., 2010, 2014; Gans et al., 2013). As discussed below, we verify that the higher-order effects only account for a negligible or minor part of the output uncertainties in our model (see Sect. 3.3). We also ensure that the sample number (5000) is sufficiently large for a satisfactory convergence of the uncertainty analysis.

AMTD
8, 3883–3932, 2015

3 Results and discussions

In this section, we characterize the O_x and HO_x radical chemistry in both OFR185 and OFR254-70 as a function of the three most important inputs: H_2O, UV, and OHR_{ext}. We also show sensitivity analysis-related results, i.e., the output uncertainties and their apportionment to the input parameters.

The cases with very high external OH reactivity ($1000\,s^{-1}$) are not representative of ambient conditions, but rather are included to represent some laboratory experiments under very high reactant concentrations (Lambe et al., 2011b, 2014; Tkacik et al., 2014; Liu et al., 2015). Only key results for these cases are discussed in detail in this section, with most results being reported in the Supplement.

3.1 Main species and conversions

OFRs have high OH concentrations and active HO_x chemistry, as shown in Fig. 1 for the case with medium H_2O and UV, and zero OHR_{ext} (case MM0, cf. Table 1). For this case, OH concentrations in both OFR185 and OFR254-70 are of the order of magnitude of 10^{10} molecules cm^{-3} and thus $\sim$ 4 orders of magnitude higher than typical ambient values (Stone et al., 2012). The O_3 and HO_2 concentrations are higher than ambient as well by several orders of magnitude. These higher concentrations of highly oxidative species are the key to the OFRs' short oxidation timescales.

The arrows in Fig. 1 indicate how HO_x species are formed, interconverted, and consumed. Both reactors form primary OH from O_3 + 254 nm, while OFR185 produces 70 % of its primary HO_x from H_2O + 185 nm. Note that the production, consumption, and interconversion of HO_x have average rates on the same order of magnitude *within* each type of OFR. This comparison reveals that the interconversion of HO_x is very active in these OFRs, even without an external OH reactant that converts OH into HO_2,

AMTD
8, 3883–3932, 2015

e.g., SO_2. This interconversion is dominated by O_3 through the following reactions:

$$O_3 + OH \rightarrow HO_2 + O_2, \quad \text{(R1)}$$

$$O_3 + HO_2 \rightarrow OH + 2O_2. \quad \text{(R2)}$$

On the other hand, the interconversion of HO_x does not dominate over its primary production and final destruction. In both OFRs, the flux of $OH \rightarrow HO_2$ is several times as large as that of $HO_2 \rightarrow OH$. This implies that, on average, for each primary HO_x produced, it does not interconvert many times, but rather relatively quickly follows its destruction pathway to form H_2O or H_2O_2.

In OFR254-70, the production, consumption, and interconversion of HO_x are all 1–2 orders of magnitude faster than in OFR185. The faster conversions in OFR254-70 result from the substantial initial injection of O_3 in OFR254-70, ~ 25 times more than the O_3 formed in OFR185 under these average conditions, as the latter is only formed internally from O_2 + 185 nm.

3.2 Characterization of the radical chemistry vs. H_2O, UV, and OHR_{ext}

In this section, we explore the radical chemistry systematically as a function of input conditions through examination of the dependence of several output and internal chemistry parameters. We systematically compare the results for OFR254-70 and OFR185 for all parameters, and interpret the reasons for the observed trends.

3.2.1 OH and O_3 exposures

Figures 2 and 3 show OH and O_3 exposures, respectively, for both reactors as a function of H_2O, UV, and OHR_{ext}. The highest OH exposures are quite close in OFR185 and OFR254-70, as are the highest O_3 exposures. The highest OH and O_3 exposures are slightly larger than 10^{13} and 10^{17} molecules cm^{-3} s, respectively. For OH_{exp} the two OFRs are similarly sensitive to the inputs under higher H_2O or UV at mid to low OHR_{ext}. OFR185 is more sensitive to the inputs at lower H_2O and UV and high OHR_{ext}.

AMTD
8, 3883–3932, 2015

OH and O_3 exposures in OFR185 can be 5 and 3 orders of magnitude lower than their highest values, respectively, over the range of conditions considered here. By contrast, in OFR254-70 the lowest OH_{exp} is only two orders of magnitude lower than its highest value, and O_3 exposure is almost independent of the explored conditions. The different dynamic ranges can be important when designing experiments across a wide range of OH_{exp}.

The difference between the O_3 exposures in OFR185 and OFR254-70 can be easily explained. O_3 in OFR254-70 depends on almost nothing but the initially injected amount, at least under the high injected amounts considered in our study (70 ppm). Only under the highest UV and H_2O conditions does O_3 destruction by photolysis and HO_x recycling reactions result in a significant decrease in the O_3 concentrations. In OFR185, primary O_3 is exclusively produced via O_2 + 185 nm. Therefore, the O_3 production in OFR185 is nearly proportional to the photon flux at 185 nm (Fig. 3b′–d′). As the 185 nm flux spans three orders of magnitude, so does the O_3 exposure. The O_3 consumption in both OFRs is minor compared to the O_3 production under most conditions. Destruction of most O_3 by photons and HO_x only occurs under conditions where UV is high and H_2O is not too low (Fig. 3a, e, b′–h′). The very different exposures to O_3 in each OFR are important when considering species that react with both OH and O_3 such as monoterpenes.

In contrast, the reasons for the difference in OH_{exp} between OFR185 and OFR254-70 are complex. OH is formed through H_2O + 185 nm and O_3 + 254 nm in OFR185, and exclusively from the latter reaction in OFR254-70. Therefore, the primary production of OH in both cases should be approximately proportional to the water vapor concentration, photon flux, and O_3 concentration. In our base case O_3 is much higher in OFR254-70, resulting in a much stronger primary OH source that makes the chemistry more resilient to external perturbation. In addition, the consumption of OH due to OHR_{ext} in both cases should be trivially proportional to OHR_{ext}. Thus, this different behavior of the OH exposures in the two OFRs should result from differences in the HO_x chemistry of the OFRs.

AMTD
8, 3883–3932, 2015

Indeed the interconversion of OH and HO_2, shown in the previous section to be greatly enhanced by the injected O_3 in OFR254-70, plays an important role on the observed differences. In cases with substantial external consumption of OH (Fig. 2c, d, g, h), the rapid interconversion of OH and HO_2 in OFR254-70 buffers the OH concentration by producing OH from the more abundant HO_2. The higher the O_3 concentration, the stronger the buffering effect. Consequently, OH_{exp} is much less sensitive to OHR_{ext} in OFR254-70 under these conditions (Fig. 2g, h), than in OFR185 (Fig. 2c, d). In other words, the recycling of OH from $O_3 + HO_2$ buffers the consumption of OH.

3.2.2 OH reactivity (OHR)

The O_3 buffering effect can be investigated more quantitatively by considering OHR, the inverse of the OH lifetime and a direct measure of OH consumption rate. OHR_{tot}, i.e., the sum of OHR_{ext} from external reactants such as SO_2 and OHR_{int} from internal reactants such as HO_2 and O_3 (including the injected O_3 in OFR254), is shown vs. operating conditions in Fig. S2. The OHR_{tot} in Fig. S2b, f is just the *internal OH reactivity*, as there is no OHR_{ext}. As expected for this case, the major components of OHR_{int} are O_3, H_2O_2, HO_2, and OH itself.

In OFR185, a strong UV dependence is observed in OHR_{int} Fig. S2b, b′: from $\sim 1\,s^{-1}$ in the low-UV cases to $\sim 100\,s^{-1}$ in the high-UV cases. H_2O has only a minor influence on OHR_{int}. At low UV and H_2O, increasing H_2O leads to a HO_x source and thus increasing OHR_{int}. In the case of high UV, a high H_2O results in increasing concentrations of HO_x that cause a significant loss of O_3 and a net decrease in OHR_{int}.

As OHR_{ext} increases, the dependence of OHR_{tot} on UV in OFR185 is weakened (Fig. S2c, d, c′, d′). We observe that OHR_{tot} is roughly equal to the sum of initial OHR_{ext} plus OHR_{int} from the case without OHR_{ext}. Although OHR_{ext} can be significantly reduced by the reaction with OH at medium and high UV, the resulting HO_2 and H_2O_2 produced from HO_2 increase OHR_{int}. Thus, the net change in OHR_{tot} is minor. However, the increase in OHR_{int} is slightly greater than the decrease in OHR_{ext}, in agreement with Li et al. (2015), as HO_2 and H_2O_2 are more reactive with OH than

AMTD
8, 3883–3932, 2015

SO_2. Therefore, at medium and high UV, the relative contribution of OHR_{int} to OHR_{tot} is significantly higher than the values estimated from initial OHR_{ext} and OHR_{int} in the case without OHR_{ext} (Fig. S3b, c, b′, c′). However, at low UV, the amount of OH is not sufficient to cause a significant consumption of SO_2 and OHR_{int} is much lower than OHR_{ext}. As a result, OHR_{ext} dominates OHR_{tot} at low UV, which explains the remarkably low OH_{exp} at low UV and high OHR_{ext} in OFR185.

In contrast to OFR185, in OFR254-70 (with 70 ppm O_3 input) OHR_{ext} never becomes dominant under the conditions of OHR_{ext} = 0–100 s^{-1} (Fig. S3d–f, e′, f′). OHR_{int} accounts for > 90 and > 50 % of OHR_{tot} for the cases with 10 and 100 s^{-1} OHR_{ext}, respectively. The amount of O_3 injected contributes OHR_{int} = 101 s^{-1}, which is in agreement with an almost uniform OHR_{int} of ∼ 100 s^{-1} in all cases except with high H_2O and UV, and the OHR_{tot} shown in Fig. S2e–h, f′–h′. At high H_2O and UV levels, in both OFR185 and OFR254-70, very large concentrations of OH radicals are formed and consume most external OH reactant, resulting in an OHR_{int} dominating OHR_{tot} (Fig. S3). Interestingly, under this condition, almost all O_3 (> 90 %) is also consumed in OFR254-70, leading to the only observed significant OHR_{tot} decrease for OFR254-70 (Fig. S2e–h, f′–h′), which, in part, contribute to the highest observed OH_{exp} reached by OFR254-70 (Fig. 2f–h, f′–h′).

3.2.3 OH suppression

The changes in OH_{exp} can also be described in terms of OH suppression, i.e., the decrease of OH concentration caused by an addition of OHR_{ext} (Li et al., 2015). OH can be greatly suppressed in OFR185 if OHR_{ext} is high (Li et al., 2015), as shown in Fig. 4a–c, b′, c′. For OHR_{ext} = 100 s^{-1}, OH suppression is larger than 80 % except for high UV cases. This is due to rapid conversion for OH to HO_2 by OHR_{ext}, while HO_2 cannot be quickly recycled back to OH due to relatively low levels of O_3. In contrast, for $OHR_{ext} \leq 100\ s^{-1}$, OH in OFR254-70 is at most suppressed by ∼ 50 %, and less for the cases with a high H_2O or UV (Fig. 4e–g, f′, g′). The injected O_3 in OFR254-70 explains

AMTD
8, 3883–3932, 2015

the large difference between the reactors: it primarily produces much OH, recycles HO_2 to OH and thus prevents the latter from being largely suppressed. Interestingly the suppression of OH is not accompanied by a suppression of total HO_x, as illustrated in Fig. S4. Total HO_x remains approximately constant in OFR254-70 independently of OHR_{ext} in the cases with OHR_{ext} =10 and 100 s^{-1}, as the fast recycling of OH and HO_2 by O_3 is predominant in the reactivity of both species. Total HO_x actually increases up to a factor of ∼ 2 in OFR185, especially on the conditions that lead to OH suppression, as OH is converted to HO_2 and the total HO_x loss is reduced.

3.2.4 OFR conditions at very high OHR_{ext}

Very high OHR_{ext} of the order 1000 s^{-1} or more has been used in some laboratory and field experiments (Lambe et al., 2011b; Tkacik et al., 2014; Liu et al., 2015), and thus it is of interest to explore the changes in OFR performance under these conditions. The chemistry in the cases with a very high OHR_{ext} (1000 s^{-1}) (Figs. S5–S9) retains all trends with increasing OHR_{ext} discussed above. O_3 is still only slightly affected by OHR_{ext} (Fig. S6). In most cases, OHR_{tot} reaches the 1000 s^{-1} level (Fig. S7), to which OHR_{ext} is the dominant contribution, since the OHR_{int} in both OFR185 and OFR254-70 only reaches ∼ 100 s^{-1}. Under high H_2O and high UV conditions, strong OH production still leads to substantial consumption of the external OH reactant, which makes the reduced OHR_{ext} comparable to OHR_{int} (Fig. S8). These trends are also consistent with the changes of OH_{exp}, which is further lowered/suppressed at OHR_{ext} of 1000 s^{-1} (Figs. S5 and S9). O_3-promoted HO_2-to-OH recycling is always pronounced and systematically makes OH in OFR254-70 more resilient to the increase of OHR_{ext}, although OH suppression still reaches a factor of 8. Total HO_x at high H_2O and UV in OFR254-70 increases by a factor of ∼ 2 (Fig. S4e, h, h′), as most O_3 is consumed and OH is converted to HO_2 by the external OH reactant. At these very high OHR_{ext}, OFR185 can only achieve substantial OH_{exp} at medium to high UV levels and is not useful at low UV levels unless very low OH_{exp} are desired. Very high OHR_{ext} also results in much

AMTD
8, 3883–3932, 2015

increased relative importance of non-OH driven reactions in both OFRs, which will be addressed in future work.

3.3 Parametric uncertainty analysis

In this section, we quantify the uncertainties on the model outputs due to the uncertainty in model parameters (rate constants and (partial) cross-sections), and compare them with the dynamic ranges of some outputs to confirm the reliability of the results shown in the previous section. With the statistical samples of uncertain inputs and outputs, we can also perform an analysis to determine the reactions that contribute the most to output uncertainties.

3.3.1 Output uncertainty

We observe, over a wide range of conditions for both OFR185 and OFR254-70 (Fig. 5), moderate uncertainties (bar heights in Fig. 5) of the four key outputs: OH_{exp}, O_3, HO_2/OH, and H_2O_2. In most cases, the relative uncertainties of these outputs (1 SD) are lower than 40 %. None of the relative uncertainties that we obtained is higher than 56 %. For the most important output, OH_{exp}, the typical relative uncertainty is 15–20 % for both OFR185 and OFR254-70, with a few cases reaching ∼ 25 %. This relative uncertainty is remarkably low and strongly suggests that the kinetic and photolysis parameters are not the dominant uncertainty sources in the system. Compared to the dynamic ranges of OH and O_3 exposures, which span ∼ 5 and ∼ 3 orders of magnitude in OFR185 and ∼ 3 and 1/2 orders of magnitude in OFR254-70, these output relative uncertainties are generally quite low. In other words, the kinetic and photolysis parameters used in this study are known well enough to ensure reliable findings of the changes in chemistry with model inputs, within the physical assumptions of the model. The uncertainties in this model compared to experiments are likely dominated by the simplifications introduced in the model (e.g., plug flow, uniform radiation field, and no wall effects), as well as by incomplete information about the experimental inputs (e.g.

AMTD
8, 3883–3932, 2015

quantification of OHR_{ext}, dependence of UV light output on ambient temperature and lamp age, etc.).

3.3.2 Reactions contributing the most to the parametric uncertainty

It is of interest to characterize which reactions substantially contribute to the output uncertainties. We consider reactions with correlation coefficients between its kinetic parameter and outputs larger than 0.2 as reactions that contribute significant uncertainty. This criterion has been previously applied for similar analyses (Hébrard et al., 2009; Peng et al., 2010). A total of 10 reactions (out of 46 included in the model) are identified as controlling the parametric uncertainty of this model. These include the photolyses of the major species (H_2O and O_2 in OFR185; O_3 in both OFRs) and reactions of OH and HO_2 with themselves or some abundant species, i.e., O_3 and H_2O_2. We have discussed the importance of OH and HO_2 reactions in the gas-phase chemistry in OFRs previously. Initiation steps such as photolysis are highly influential in complex reaction networks (Peng et al., 2010). Thus, it is natural that these reactions appear as key contributors.

The photolyses of H_2O and O_2, which are the main pathways of primary OH and O_3 production in OFR185, respectively, are generally the most important contributors to the parametric uncertainty in OH_{exp} and O_3, respectively. O_3 + 254 nm also contributes to the uncertainty of both parameters in some cases. HO_2/OH and H_2O_2, which involve non-primary products, are significantly influenced by more reactions in OFR185 compared to OH_{exp} and O_3, some of the most important being HO_2 + HO_2 and OH + O_3.

In OFR254-70, OH is not produced by photolysis of H_2O, but only O_3 + 254 nm. Therefore, photolysis of ozone is always an important contributor to the uncertainty on OH_{exp}. The reaction OH + O_3 is typically of comparable magnitude to O_3 photolysis, with the reactions HO_2 + O_3 and HO_2 self-reaction typically comprising the balance. Because of the large amount of O_3 injected and since input uncertainties are not considered in this analysis, O_3 (at the exit of the reactor) has very low parametric uncertainty,

AMTD
8, 3883–3932, 2015

except for cases with high H_2O and UV where a larger fraction of the injected O_3 is consumed by photons. HO_2/OH and H_2O_2 also have many uncertainty contributions, as in OFR185, with the most important for HO_2/OH being $OH + O_3$, $HO_2 + O_3$ and sometimes (high UV and H_2O) O_3 photolysis and $OH + HO_2$. The largest contributors to the uncertainty of modeled H_2O_2 are the HO_2 and OH self-reactions, with smaller contributions from $OH + O_3$, $OH + H_2O_2$, and O_3 photolysis, but with quite variable proportions for the different cases. In OFR254-70, the recycling of HO_2 to OH is of remarkably higher importance than in OFR185, especially for OH_{exp} and HO_2/OH, which are the outputs directly affected by these conversions.

3.4 Effects of several additional parameters

In addition to the major parameters altering the OFR radical chemistry (i.e., H_2O, UV, and OHR_{ext}), we investigate here the effects of some other parameters, i.e., difference between non-destructive and destructive OHR_{ext} (in terms of HO_x), the identity of external OH reactants, and the amount of injected O_3 in OFR254, by comparison with the base case, i.e., the case studied in Sect. 3.2.

3.4.1 Non-HO_x-destructive vs. HO_x-destructive OHR_{ext}

The consumption of OH by SO_2 leads to the production of HO_2, which does not lower the total amount of HO_x. Although this HO_2 regeneration also extensively exists in VOC oxidation, it is important to have a better understanding on the impact of destructive external OH reactants, i.e., external OH reactants whose OH-consuming process is not coupled with HO_2 regeneration, e.g., $OH + NO_2 + M \rightarrow HNO_3 + M$, an important reaction in the OFR of Tkacik et al. (2014) because of the presence of large amount of NO_x in the source air in their study. To more clearly isolate the effect of HO_x-destructive vs. non-HO_x-destructive OHR_{ext}, we use SO_2 as the external OH reactant for both cases, but for the probing of the HO_x-destructive OHR_{ext} assume that the HO_2 regeneration reaction $HSO_3 + O_2 \rightarrow SO_3 + HO_2$ does not occur.

AMTD
8, 3883–3932, 2015

The absence of HO_2 regeneration has mostly minor effects on OH_{exp}, as shown in Fig. 6, except for OFR254-70 at low UV and both OFRs at high H_2O and UV and very high OHR_{ext}. For OFR185 (Fig. 6a–d, b′–d′), under most conditions, OH_{exp} is very close to the value in the base case (Fig. 2). At the highest UV and $OHR_{ext} \leq 100\,s^{-1}$, photolysis dominates OH production, while the contribution of the recycling of HO_2 generated from SO_2 consumption to OH is small. At low UV, OH production from photolysis is weak, but the recycling of HO_2 generated from SO_2 consumption to OH becomes even weaker because of not only less OH that can be converted into HO_2 by SO_2, but also less O_3 that can recycle HO_2 to OH. Only under two particular conditions: (i) at high H_2O, high OHR_{ext} and UV at 185 nm around 3×10^{13} photons $cm^{-2}\,s^{-1}$, and (ii) at high H_2O and UV and very high OHR_{ext}, a significant increase in OH_{exp} relative to the base case is observed (Fig. 6c, d, c′, d′), because the reduced OH consumption by the lower HO_2 and H_2O_2 is important under these conditions.

For OFR254-70, under low-OHR_{ext} conditions, OH production by photolysis is high enough and/or HO_2 regeneration coupled with SO_2 consumption is low enough to prevent the regeneration of HO_2 from being a major effect (Fig. 6e–h, f′–h′). However, at low H_2O, low UV, and high/very high OHR_{ext}, the lack of HO_2 production from OHR_{ext} does cause a significantly lower OH_{exp} (Fig. 6e, g, h, g′, h′), because under these conditions the reduction in OH recycling by $HO_2 + O_3$ is important. This effect can reach an order-of-magnitude at the lowest UV. In addition, at high H_2O and UV and very high OHR_{ext}, OH_{exp} increases significantly relative to the corresponding base case, for the same reason as in OFR185.

3.4.2 Identity of external OH reactants

The use of SO_2 as the surrogate of external OH reactants is a simplification in this study. In actual OFR experiments, external OH reactants can also be NO_x, CO, CH_4, and various VOC and their oxidation products. These reactants have a wide range of rate constants with OH, and the relative decrease of OHR_{ext} with time in the OFR can

AMTD
8, 3883–3932, 2015

thus vary substantially between these cases. To bound the importance of this effect we study two extreme regimes, i.e., one where OHR_{ext} does not decay at all, and one where the external OH reactant is consumed at the collision rate. In both cases the products of the initial reaction are not explicitly represented in the model. For VOC reactions the former case is more realistic, as the constant OHR_{ext} can be thought to represent the reactivity of several generations of products as the initial reactant is consumed.

The effects of this parameter are shown in Figs. S10 and S11, and can be understood in terms of the impact of OHR_{ext} on reducing OH_{exp} illustrated in Figs. 2 and 4. When using a constant OHR_{ext} instead of SO_2 (Fig. S10), OH_{exp} is reduced similarly in both OFR for high UV and H_2O conditions. These were the conditions where a substantial fraction of the injected SO_2 was consumed in the reactor, thus keeping OHR_{ext} constant instead leads to up to factors of 2–3 reduction in OH_{exp}. The effect increases with OHR_{ext} as expected.

The effect of replacing SO_2 with a reactant with a collision-rate reaction is more dramatic (Fig. S11), but can be similarly understood. Note that to achieve the same initial OHR_{ext}, the concentration of the reactant is ~ 300 times lower than for the SO_2 case. Therefore the reactant is quickly consumed at short reaction times and for the rest of the residence time the OFRs revert to conditions with low OHR_{ext} (e.g. Fig. 2b, f). Thus, the integrated OH concentration, i.e., OH_{exp} is still suppressed relative to the no OHR_{ext} case but not as much as if all the OHR_{ext} is due to SO_2. In particular, OH_{exp}, increases strongly in the cases in which OH suppression was important and when the consumption of external OH reactant is significant, i.e., OFR185 at relatively low UV and/or H_2O but not at the lowest UV and H_2O. The effect reaches a factor of ~ 40 for OFR185 but only ~ 2 for OFR254-70, consistent with the much larger OH suppression in the former.

In summary, the identity of the OH reactant can make a substantial difference on OH_{exp} for OFR185 and very fast reacting species, and less so for other cases. However, note that this substantial difference is likely an artifact due to our simplified modeling

AMTD
8, 3883–3932, 2015

for this case. In our model, there is no regeneration of external OH reactant (SO_2) after its consumption, while in reality, no VOC can be completely oxidized in only one step and most VOC oxidation intermediates also act as external OH reactants. Thus, it is very unlikely that OHR_{ext} in real cases can drop as quickly as shown in this case, even though the primary oxidation rate of some VOCs (e.g., isoprene) can be close to the collision rate.

3.4.3 Amount of injected O_3 in OFR254

The amount of injected O_3 is also a factor that may alter the chemistry in OFR254. In the BEACHON-RoMBAS campaign (Palm et al., 2015), 70 ppm O_3 was used in OFR254 to ensure reaching high OH exposures, while O_3 in Kang et al., and Lambe et al.'s laboratory studies (Kang et al., 2011; Lambe et al., 2011b) was 9 and 27 ppm, respectively. Thus, it is of interest to investigate the effect of a lower amount of injected O_3 on the OFR254 chemistry (compared to the base case of 70 ppm used in all other model runs in our study).

The ratio of OH_{exp} vs. H_2O, UV, and OHR_{ext} in OFR254-7 vs. OFR254-70 is shown in Fig. 7. At 0 OHR_{ext} (Fig. 7b, b′), OH_{exp} is ∼ 40–80 % of that in the base case, despite a lower initial O_3 concentration by a factor of 10. This minor difference is due to both OH production and consumption that are slowed down simultaneously: with less O_3, OH production through O_3 photolysis is weaker, although less than linearly as the UV light is less attenuated by the lower O_3. OH consumption by internal OH reactants, e.g., O_3, HO_2, and H_2O_2, is also weaker, because of less HO_2 formation through $OH + O_3 \rightarrow HO_2 + O_2$, as well as lower H_2O_2 formation.

However, as OHR_{ext} increases, SO_2 contributes increasingly to OH consumption. The case with $OHR_{ext} = 10\,s^{-1}$ gives similar results to the one without OHR_{ext}, as the OHR_{int} from O_3 is also $10\,s^{-1}$, and the reactor chemistry is not overwhelmed by OHR_{ext}. However when $OHR_{ext} = 100$ (Fig. 7d, d′) and $1000\,s^{-1}$ (Fig. S12), the external reactivity does overwhelm the internal one, and strong OH suppression up to 2 orders of

AMTD
8, 3883–3932, 2015

magnitude is observed, similar to what was discussed above for some conditions in OFR185. OH primary production from O_3 + 254 nm and its recycling from $O_3 + HO_2$ are smaller compared to the consumption by SO_2.

3.5 Summary of the relationship between OH suppression and OHR_{ext}

In the discussions above, we have seen several cases where OH suppression in OFR254 is regulated by both O_3 and OHR_{ext}. At $OHR_{ext} \leq 100\,s^{-1}$ in OFR254-70 ($OHR_{O_3} = 101\,s^{-1}$), O_3-promoted interconversion of HO_x is highly active and a comparable or smaller amount of OHR_{ext} cannot significantly perturb this recycling. Therefore, OH concentration remains relatively stable with increasing OHR_{ext}, leading to negligible or small OH suppression. When OHR_{ext} is $\gg 100\,s^{-1}$ in OFR254-70, the steady state between OH and HO_2 due to their interconversion is overwhelmingly shifted toward HO_2 by the large amounts of external OH reactant. In other words, OH is strongly suppressed. In OFR254-7 ($OHR_{O_3} = 10\,s^{-1}$), the HO_x interconversion is less resilient to OHR_{ext}. A $100\,s^{-1}$ OHR_{ext} can already greatly affect this interconversion and lead to strong OH suppression.

These facts suggests that OH suppression in OFR254 depends on OHR_{int} due to O_3, OHR_{O_3}, relative to OHR_{ext}. We thus investigate the dependence of OH suppression on the ratio OHR_{O_3}/OHR_{ext}. Such a relationship is summarized in Fig. 8 for not only OFR254 (OFR254-70 and OFR254-7), but also OFR185, as the resilience of OH_{exp} to OHR_{ext} in OFR185 also stems from O_3-promoted HO_x recycling.

OH suppression is negligible if $OHR_{O_3}/OHR_{ext} \gg 1$. As this ratio decreases towards 1, we observe a regime change, where OH_{exp} begins to significantly decrease compared to the cases without OHR_{ext}. After that, percentage of remaining OH after suppression (rOH_{exp}) exhibits a nearly exponential decrease with decreasing

AMTD
8, 3883–3932, 2015

OHR_{O_3}/OHR_{ext}. This trend can be fitted by a sigmoid of $\log(OHR_{O_3}/OHR_{ext})$, i.e.,

$$rOH_{exp} = \frac{100}{1 + \exp\left(\frac{x_0 - \log(OHR_{O_3}/OHR_{ext})}{s}\right)}, \quad (4)$$

where x and s are fitting parameters. s measures the steepness of the increasing part of the curve: the smaller s, the steeper the curve. For OFR185 $x = -0.021$ and $s = 0.638$, while for OFR254 (fitted from both OFR254-70 and OFR254-7 data) $x = -0.155$ and $s = 0.445$. The steeper OH suppression for OFR254 reflects a generally faster decrease of remaining OH after suppression with decreasing O_3 and/or increasing OHR_{ext}. In other words, in cases with significant OH suppression, OH in OFR254 is usually more suppressed than in an OFR185 at the *same* OHR_{O_3}/OHR_{ext}, as shown in Fig. 8. This can be explained by the fact that for the same value of OHR_{O_3}/OHR_{ext}, OHR_{O_3} and OHR_{ext} in OFR185 are usually smaller than in OFR254, as O_3 in OFR185 generally cannot be as high as injected in OFR254 unless at very high UV.

This relationship between OH suppression and OHR_{O_3}/OHR_{ext} holds not only for SO_2 as OH reactant, but also for real primary VOCs and their oxidation intermediates. We observe the same trend for the cases with external OH reactant surrogates reacting with OH at 0 (constant OHR_{ext}) – 1.8×10^{-10} cm^3 $molecules^{-1}$ (collision rate) as for the base case with SO_2 (Fig. S13). For both OFR185 and OFR254, data points of all external OH reactant surrogates in the whole explored H_2O, UV, and OHR_{ext} range are in a very narrow corridor showing the above-mentioned trend. In the case of a faster OH reactant decay, average OHR_{ext} is lower, which leads to both higher rOH_{exp} and OHR_{O_3}/OHR_{ext}. The point corresponding to this case shifts toward upper right in Fig. S13, but is still located in the corridor. We can similarly rationalize the case of a slower OH reactant decay. The results in Fig. S13 suggest that even in the case of real VOC oxidation in OFR, where OH reactants are various and OHR_{ext} variation is highly complex, OH suppression still follows the relationship proposed herein.

AMTD
8, 3883–3932, 2015

We also estimate the ranges of rOH_{exp} and OHR_{O_3}/OHR_{ext} of some previous OFR experiments (Fig. 8), including two series of OFR254 laboratory experiments (Kang et al., 2011; Lambe et al., 2011b) and a source study in an urban tunnel using OFR185 (Tkacik et al., 2014). In the estimation, we always use SO_2 as the VOC surrogate, since SO_2 is relatively realistic in terms of effective OHR_{ext} vs. time, as justified in Sect. 2.1. In the above-mentioned studies, as well as many other OFR studies, high OHR_{ext} was often present, while input O_3 in OFR254 and UV in OFR185 were usually not very high, leading to relatively low OHR_{O_3}/OHR_{ext}. Most estimated values of OHR_{O_3}/OHR_{ext} of these experiments fall into the regime where OH suppression is significant (estimated remaining OH range 2.5–30 %) and sensitive to OHR_{O_3}/OHR_{ext}. This suggests that unless OH_{exp} is calibrated during the relevant experiments by measuring the decay of a reactant, O_3 and OHR_{ext} need to be known to estimate the extent of OH suppression. Using OH_{exp} measured under low OHR_{ext} conditions for experiments at high OHR_{ext} can lead to more than an order-of-magnitude error in the estimated OH_{exp}, even if UV and H_2O are kept constant.

Note that the rOH_{exp} ranges estimated above are based on SO_2 (reaction rate constant with OH: 9.185×10^{-13} cm^3 $molecules^{-1}$ s^{-1}) as VOC surrogate. Employing a VOC decaying more slowly than SO_2 (e.g., CH_4) leads to similar OH suppression, as shown by the case with constant OHR_{ext} (Sect. 3.4.2). However, in the case of a VOC decaying faster than SO_2, some significant discrepancies may arise. Assuming a VOC consumed by OH at 1×10^{-11} cm^3 $molecules^{-1}$ s^{-1} without downstream oxidation, which is already unrealistic, we estimate that the difference in average OHR_{ext} between this case and the SO_2 case can be up to ~ 10 (with an OH_{exp} larger than 3×10^{12} molecules cm^{-3} s^{-1}, destroying almost all OH reactant in both cases). Then the resulting difference in rOH_{exp} can be estimated by Eq. (4). rOH_{exp} in this case can be up to ~ 5 and ~ 10 times higher than in the SO_2 case. However, these larger differences occur only if the initial OHR_{ext} is high enough to cause significant OH suppression, and OH_{exp} is high enough to consume most OH reactant. Under most conditions, the differences

AMTD
8, 3883–3932, 2015

between the two cases are within a factor of 2 and 3 for OFR185 and OFR254, respectively.

3.6 Equations for estimating OH_{exp} in OFR254

Li et al. (2015) discussed the usefulness of an estimation equation for OH_{exp} for OFR, for both laboratory and especially field experiments. An equation was reported for OFR185 in which OH_{exp} is estimated from H_2O and OHR_{ext} inputs and O_3 output, with the latter parameter serving as a surrogate of UV (Li et al., 2015). In this study, we expand upon the previous work by deriving estimation equations for OFR254.

3.6.1 Estimation equation for OH_{exp} as a function of H_2O, UV, OHR_{ext}, and $O_{3,in}$

As discussed in the previous subsection, besides H_2O, UV, and OHR_{ext}, the amount of initially injected O_3 in OFR254 ($O_{3,in}$) also has a major impact on OH_{exp}. First, we derive an estimation equation of OH_{exp} as a function of these 4 variables based on all OH_{exp} data points that we calculated in the explored range of H_2O (0.0007–0.023, 30 linearly evenly spaced points), UV (4.2×10^{13}–8.5×10^{15} photons $cm^{-2}\,s^{-1}$ at 254 nm, 30 points corresponding to exponentially evenly spaced points of UV at 185 nm between 10^{11}–10^{14} photons $cm^{-2}\,s^{-1}$), and OHR_{ext} (1 point at $0\,s^{-1}$ and 31 exponentially evenly spaced points in the range of 1–1000 s^{-1}), as well as the range of $O_{3,in}$ between 7 and 70 ppm (11 exponentially evenly spaced points). In total 316800 data points obtained from the base case of the model (non-HO_x-destructive SO_2 as surrogate of external OH reactant) are used to derive the following estimation equation:

$$\log OH_{exp} = a + b_1 \log H_2O + b_2(\log H_2O)^2 + c_1 \log UV + c_2(\log UV)^2 - \log\left(1 + \exp\left(\frac{d - \log\left(O_{3,in}/OHR_{ext}\right)}{e}\right)\right), \quad (5)$$

AMTD
8, 3883–3932, 2015

where H_2O (water mixing ratio) is unitless, and OH_{exp}, UV, OHR_{ext}, and $O_{3,in}$ are in molecules cm^{-3} s, photons cm^{-2} s^{-1}, s^{-1}, and ppm, respectively. a, b_1, b_2, c_1, c_2, d, and e are fitting parameters. The equation is composed of a part of OH_{exp} at 0 OHR_{ext} (first row) and a part representing OH suppression (second row), which is very similar to Eq. (4). Considering the non-linearity of the model response, we use 2 terms for each variable that has major influence on OH_{exp} in the case without OHR_{ext}, i.e., H_2O and UV. The fitting parameters (Table S1) are obtained by fitting Eq. (5) to the OH_{exp} model results that we calculate using the model in the variable space spanned by H_2O, UV, OHR_{ext}, and $O_{3,in}$. Figure 9a shows the comparison between OH_{exp} calculated from the full model and estimated by Eq. (5). Most estimated OH_{exp} data points are within a factor of 2 from the full model OH_{exp}. The mean absolute value of the relative deviation is 15 % (Fig. 9a), which is smaller than the parametric uncertainly of the model discussed above. The satisfactory performance of Eq. (5) demonstrates its applicability to OFR254 under a very wide range of conditions.

However, this applicability may be constrained by the UV flux, the variable in Eq. (5) that is most difficult to measure. For OFRs using the same lamps and power supplies as in our laboratory, we provide with a UV-flux to lamp voltage relationship (Fig. S14) that allows estimating UV from lamp voltage. This equation is based on UV flux vs. lamp setting relationship reported by Li et al. (2015), and the lamp setting-lamp voltage relationship from our group's previous measurements. This result allows the application of Eq. (5) to PAM OFRs and others using the same lamps. However, the fluxes reported in Li et al. (2014) represent the average or "effective" flux throughout the reactor, and the output of individual Hg lamps may vary depending on the lamp, its age and usage, and possibly its temperature. As a consequence, there is a substantial uncertainty in the UV flux estimated from lamp voltages. An alternative method to estimate OH_{exp} without using the estimated UV flux is thus desirable.

AMTD
8, 3883–3932, 2015

3.6.2 Estimation equation for OH_{exp} as a function of rO_3, OHR_{ext}, and $O_{3,in}$

The OH_{exp} estimation equation proposed by Li et al. (2015) for OFR185 avoided an explicit dependence on UV by using instead O_3 as its surrogate, since in OFR185 this species is only created by the 185 nm radiation. We follow a similar approach to derive an alternative estimation equation for OH_{exp} in OFR254 in which the ratio of the output to input O_3 ($rO_3 = O_{3,out}/O_{3,in}$) is used as a surrogate of UV, as well as H_2O, since both photons and HO_x produced from H_2O destroy O_3. OH_{exp} can then be expressed as a function of only rO_3, OHR_{ext}, and $O_{3,in}$:

$$\log OH_{exp} = a - \log rO_3 + b(OHR_{ext}/O_{3,in})^c, \quad (6)$$

where a–c are fitting parameters. Their values are reported in Table S1. Obviously, Eq. (6), with only 3 input variables and 5 parameters, is much simpler than Eq. (5). Furthermore, the mean absolute value of the relative deviation between OH_{exp} estimated by Eq. (6) and computed by the full model is only 9 %, and the scatter in the relationship is substantially smaller than for Eq. (5) (Fig. 9b). O_3 can be easily monitored in OFR254 experiments at both the entrance and the exit of the OFR with a single O_3 analyzer and a switching valve system. Therefore, we recommend measuring both O_3 input and output concentrations in OFR254 experiments to more simply and accurately estimate OH_{exp}. Note that a good experimental determination of rO_3 requires that a measurable amount of O_3 is destroyed, but also that some O_3 still remains at the reactor output. We estimate this range as corresponding to rO_3 between 0.05 and 0.95. However, $rO_3 > 0.95$ (i.e., only < 5 % of $O_{3,in}$ is destroyed in the OFR) only occurs under low H_2O and/or UV conditions, where OH_{exp} is also very low and may be of limited experimental interest, while $rO_3 < 0.05$ occurs rarely, i.e., only at the highest H_2O and UV that we explored. For experiments where rO_3 is very low or close to 1, Eq. (5) can be applied to estimate OH_{exp}.

The good performance of Eq. (6) can be explained by a key relationship between OH_{exp} and rO_3. Note that the last term in Eq. (6) are minor: $b(OHR_{ext}/O_{3,in})^c$ generally

AMTD
8, 3883–3932, 2015

ranges 0.5–1, while rO_3 spans 3 orders of magnitude. Thus, log OH_{exp} is approximately proportional to log rO_3, which already captures effects of both H_2O and UV, as well as partial effects of OHR_{ext} and $O_{3,in}$. The last term in Eq. (6) can be regarded as a minor correction. Using the destruction of O_3 is conceptually similar to estimating OH_{exp} by measuring the decay of conventional OH reactants, e.g., SO_2 and CO. To estimate OH_{exp}, we utilize the relationship that the loss of reactant molecules is proportional to OH_{exp} and their rate constant. However, when O_3 destruction is used as the basis for OH_{exp} estimation, the relationship is somewhat different. An approximate proportional relationship still holds between consumed OH and O_3, hence also between OH_{exp} and rO_3.

Note that both estimation equations are based on SO_2 as VOC surrogate. Although not common, both equations may lead to a significant underestimation in OH_{exp}, if effective OH reactant decays significantly faster than SO_2 in an experiment. In this case, a correction factor can be estimated by Eq. (4) according to the external OH reactant decay rates, as described in Sect. 3.5.

4 Conclusions

We performed a systematic modeling study of the O_x and HO_x radical chemistry in OFR185 and OFR254 as a function of H_2O mixing ratio, UV photon flux, and external OH reactivity. In general, the higher H_2O mixing ratio and UV photon flux and/or the lower external OH reactivity, the higher OH exposure in OFRs.

Active OH-to-HO_2 recycling was observed in the system and is much stronger in OFR254 with 70 ppm O_3 injected as simulated here because a large amount of injected O_3 promotes both sides of this interconversion in OFR254. Strong OH production and OH-to-HO_2 recycling due to injected O_3 leads to a greater resilience of the chemistry in OFR254 to the suppression of OH by external OH reactivity. In OFR185, OH can be ~ 100 % suppressed at low H_2O mixing ratio, low UV photon flux, and high external OH reactivity, while ~ 50 % OH remains in OFR254 under the same condition. However

AMTD
8, 3883–3932, 2015

when OFR254 is used with lower input O_3 levels as done in many studies, similarly large OH suppression as in OFR185 is observed due to the inability of O_3 to recycle HO_2 to OH at a sufficient rate.

An uncertainty analysis of this chemistry based on Monte Carlo uncertainty propagation and correlation analysis was performed. The relative uncertainty of OH exposure due to uncertain rate constants and photolysis parameters is 25 % or less. The uncertainties of other key model outputs (O_3 concentration, ratio between HO_2 and OH exposures, and H_2O_2 concentration) are at most ~ 40 %. Compared to the dynamic range of OH exposure and O_3 concentration (3–5 orders of magnitude), these small parametric uncertainties indicate that the chemical parameters are known well enough for the purposes of OFR modeling, and that other simplifications in the model (e.g., uniform radiation field, plug flow) may contribute more to the model uncertainty. The reactions contributing the most output uncertainties were identified by uncertainty analysis. These reactions are photolysis of O_3, O_2, and H_2O and reactions of OH and HO_2 with themselves or some abundant species, i.e., O_3 and H_2O_2.

Switching to HO_x-destructive external OH reactivity was found to have a moderate impact on OH exposure under most conditions. At low H_2O mixing ratio, low UV photon flux, and high external OH reactivity, using HO_x-destructive external OH reactants instead of non-destructive ones (that regenerate HO_x) can result in a significantly lower OH exposure. Changing the identity of the external OH reactant (i.e., its rate constant of reactions with OH) while keeping the input external OH reactivity constant can result in major changes in OH exposure. Reactants with high rate constants decay quickly and reduce OHR_{ext} at later times in the reactor if corresponding products are not considered as external OH reactivity. Those reactants results in increased OH exposure.

OH suppression in OFR254 is shown to be very sensitive to the amount of injected O_3 in OFR254. This can be understood in terms of the internal OH reactivity provided by O_3. When internal OH reactivity is larger or similar to external OH reactivity, the chemistry is resilient to the external perturbation. However when external OH reactivity is much larger than internal OH reactivity, the recycling of OH via $HO_2 + O_3 \rightarrow OH + O_2$

AMTD
8, 3883–3932, 2015

is too slow and major OH suppression is observed. As many OFR studies have been conducted in that regime, this finding has important implications for their interpretation. Use of measurements under low external OH reactivity to estimate OH exposure at high external OH reactivity can lead to errors exceeding an order-of-magnitude.

We derived two estimation equations for OH exposure in OFR254 over a very wide range of H_2O concentration, UV photon flux, external OH reactivity, and initial O_3 concentration. The input parameters of the two equations are H_2O, UV, OHR_{ext}, and initial O_3 concentration, and of O_3 loss ratio, external OH reactivity, and initial O_3 concentration, respectively. The latter equation avoids the need to estimate effective UV photon flux that is difficult to determine accurately, and also more closely captures the model-calculated OH exposure (mean absolute value of the relative deviation: 10 vs. 15 %). Thus, measuring O_3 concentrations at both OFR's entrance and the exit is recommended for more accurate exposure estimation. The method demonstrated here can be used to derive modified estimation equations under conditions different than those considered here, e.g. with lower HO_2 recycling or different evolution of OHR_{ext} in the reactor than when using SO_2 as the reactant, or when using different UV sources.

As our study is systematic and covers a very large range of conditions, it not only provides more reliable insights into the gas-phase chemistry in OFRs, but also shows that OFR radical chemistry is controllable by regulating experimental conditions and predictable by modeling. Our findings will help the experimental design and the interpretation of results in future OFR studies, which would benefit OFR users in atmospheric research, e.g., SOA formation and aging, as well as those employing OFRs for other purposes, e.g., pollution scrubbing. Our results may also contribute to the design of OFRs with better properties in the future.

The Supplement related to this article is available online at doi:10.5194/amtd-8-3883-2015-supplement.

AMTD
8, 3883–3932, 2015

Acknowledgements. We thank the PAM user community as well as Weiwei Hu, and Amber Ortega for useful discussions. This research was partially supported by CARB 11-305, DOE (BER/ASR program) DE-SC0011105, and NSF AGS-1243354 & AGS-1360834. R. Li and B. B. Palm acknowledge CIRES Graduate Student Fellowships. B. B. Palm is grateful for a Graduate Fellowship from US EPA STAR (FP-91761701-0).

References

Andreozzi, R., Caprio, V., Insola, A., and Marotta, R.: Advanced oxidation processes (AOP) for water purification and recovery, Catal. Today, 53, 51–59, doi:10.1016/S0920-5861(99)00102-9, 1999.

Bahreini, R., Middlebrook, A. M., Brock, C. A., de Gouw, J. A., McKeen, S. A., Williams, L. R., Daumit, K. E., Lambe, A. T., Massoli, P., Canagaratna, M. R., Ahmadov, R., Carrasquillo, A. J., Cross, E. S., Ervens, B., Holloway, J. S., Hunter, J. F., Onasch, T. B., Pollack, I. B., Roberts, J. M., Ryerson, T. B., Warneke, C., Davidovits, P., Worsnop, D. R., and Kroll, J. H.: Mass spectral analysis of organic aerosol formed downwind of the Deepwater Horizon oil spill: field studies and laboratory confirmations, Environ. Sci. Technol., 46, 8025–8034, doi:10.1021/es301691k, 2012.

BIPM, IEC, IFCC, ILAC, ISO, IUPAC and IUPAPOIML: JCGM 101: 2008 Evaluation of measurement data – Supplement 1 to the "Guide to the expression of uncertainty in measurement" – Propagation of distributions using a Monte Carlo method, available at: http://www.bipm.org/utils/common/documents/jcgm/JCGM_101_2008_E.pdf (last access: March 2015), 2008.

Carlton, A. G., Wiedinmyer, C., and Kroll, J. H.: A review of Secondary Organic Aerosol (SOA) formation from isoprene, Atmos. Chem. Phys., 9, 4987–5005, doi:10.5194/acp-9-4987-2009, 2009.

Carter, W. P. L., Cocker, D. R., Fitz, D. R., Malkina, I. L., Bumiller, K., Sauer, C. G., Pisano, J. T., Bufalino, C. and Song, C.: A new environmental chamber for evaluation of gas-phase chemical mechanisms and secondary aerosol formation, Atmos. Environ., 39(40), 7768–7788, doi:10.1016/j.atmosenv.2005.08.040, 2005.

Cocker, D. R., Flagan, R. C., and Seinfeld, J. H.: State-of-the-art chamber facility for studying atmospheric aerosol chemistry, Environ. Sci. Technol., 35, 2594–2601, 2001.

AMTD
8, 3883–3932, 2015

Cubison, M. J., Ortega, A. M., Hayes, P. L., Farmer, D. K., Day, D., Lechner, M. J., Brune, W. H., Apel, E., Diskin, G. S., Fisher, J. A., Fuelberg, H. E., Hecobian, A., Knapp, D. J., Mikoviny, T., Riemer, D., Sachse, G. W., Sessions, W., Weber, R. J., Weinheimer, A. J., Wisthaler, A., and Jimenez, J. L.: Effects of aging on organic aerosol from open biomass burning smoke in aircraft and laboratory studies, Atmos. Chem. Phys., 11, 12049–12064, doi:10.5194/acp-11-12049-2011, 2011.

Danet, A. F., Bratu, M.-C., Radulescu, M.-C., and Bratu, A.: Portable minianalyzer based on cold vapor atomic absorption spectrometry at 184.9 nm for atmospheric mercury determination, Sensors Actuators B Chem., 137, 12–16, doi:10.1016/j.snb.2008.12.065, 2009.

Environment Canada: National Ambient Levels of Ozone, available at: https://www.ec.gc.ca/indicateurs-indicators/default.asp?lang=en&n=9EBBCA88-1 (last access: April 2015), 2014.

Gans, B., Peng, Z., Carrasco, N., Gauyacq, D., Lebonnois, S., and Pernot, P.: Impact of a new wavelength-dependent representation of methane photolysis branching ratios on the modeling of Titan's atmospheric photochemistry, Icarus, 223, 330–343, doi:10.1016/j.icarus.2012.11.024, 2013.

George, I. J., Vlasenko, A., Slowik, J. G., Broekhuizen, K., and Abbatt, J. P. D.: Heterogeneous oxidation of saturated organic aerosols by hydroxyl radicals: uptake kinetics, condensed-phase products, and particle size change, Atmos. Chem. Phys., 7, 4187–4201, doi:10.5194/acp-7-4187-2007, 2007.

Hallquist, M., Wenger, J. C., Baltensperger, U., Rudich, Y., Simpson, D., Claeys, M., Dommen, J., Donahue, N. M., George, C., Goldstein, A. H., Hamilton, J. F., Herrmann, H., Hoffmann, T., Iinuma, Y., Jang, M., Jenkin, M. E., Jimenez, J. L., Kiendler-Scharr, A., Maenhaut, W., McFiggans, G., Mentel, Th. F., Monod, A., Prévôt, A. S. H., Seinfeld, J. H., Surratt, J. D., Szmigielski, R., and Wildt, J.: The formation, properties and impact of secondary organic aerosol: current and emerging issues, Atmos. Chem. Phys., 9, 5155–5236, doi:10.5194/acp-9-5155-2009, 2009.

Hanna, S. R., Lu, Z., Frey, H. C., Wheeler, N., Vukovich, J., Arunachalam, S., Fernau, M., and Hansen, D. A.: Uncertainties in predicted ozone concentrations due to input uncertainties for the UAM-V photochemical grid model applied to the July 1995 OTAG domain, Atmos. Environ., 35, 891–903, doi:10.1016/S1352-2310(00)00367-8, 2001.

AMTD
8, 3883–3932, 2015

Hébrard, E., Dobrijevic, M., Bénilan, Y., and Raulin, F.: Photochemical kinetics uncertainties in modeling Titan's atmosphere: a review, J. Photochem. Photobiol. C Photochem. Rev., 7, 211–230, doi:10.1016/j.jphotochemrev.2006.12.004, 2006.

Hébrard, E., Dobrijevic, M., Pernot, P., Carrasco, N., Bergeat, A., Hickson, K. M., Canosa, A., Le Picard, S. D., and Sims, I. R.: How measurements of rate coefficients at low temperature increase the predictivity of photochemical models of Titan's atmosphere, J. Phys. Chem. A, 113, 11227–11237, doi:10.1021/jp905524e, 2009.

Johnson, M. S., Nilsson, E. J. K., Svensson, E. A., and Langer, S.: Gas-phase advanced oxidation for effective, efficient in situ control of pollution, Environ. Sci. Technol., 48, 8768–8776, doi:10.1021/es5012687, 2014.

Kang, E., Root, M. J., Toohey, D. W., and Brune, W. H.: Introducing the concept of Potential Aerosol Mass (PAM), Atmos. Chem. Phys., 7, 5727–5744, doi:10.5194/acp-7-5727-2007, 2007.

Kang, E., Toohey, D. W., and Brune, W. H.: Dependence of SOA oxidation on organic aerosol mass concentration and OH exposure: experimental PAM chamber studies, Atmos. Chem. Phys., 11, 1837–1852, doi:10.5194/acp-11-1837-2011, 2011.

Kumata, K., Itoh, U., Toyoshima, Y., Tanaka, N., Anzai, H., and Matsuda, A.: Photochemical vapor deposition of hydrogenated amorphous silicon films from disilane and trisilane using a low pressure mercury lamp, Appl. Phys. Lett., 48, 1380, doi:10.1063/1.96915, 1986.

Lambe, A. T., Ahern, A. T., Williams, L. R., Slowik, J. G., Wong, J. P. S., Abbatt, J. P. D., Brune, W. H., Ng, N. L., Wright, J. P., Croasdale, D. R., Worsnop, D. R., Davidovits, P., and Onasch, T. B.: Characterization of aerosol photooxidation flow reactors: heterogeneous oxidation, secondary organic aerosol formation and cloud condensation nuclei activity measurements, Atmos. Meas. Tech., 4, 445–461, doi:10.5194/amt-4-445-2011, 2011a.

Lambe, A. T., Onasch, T. B., Massoli, P., Croasdale, D. R., Wright, J. P., Ahern, A. T., Williams, L. R., Worsnop, D. R., Brune, W. H., and Davidovits, P.: Laboratory studies of the chemical composition and cloud condensation nuclei (CCN) activity of secondary organic aerosol (SOA) and oxidized primary organic aerosol (OPOA), Atmos. Chem. Phys., 11, 8913–8928, doi:10.5194/acp-11-8913-2011, 2011b.

Lambe, A. T., Onasch, T. B., Croasdale, D. R., Wright, J. P., Martin, A. T., Franklin, J. P., Massoli, P., Kroll, J. H., Canagaratna, M. R., Brune, W. H., Worsnop, D. R., and Davidovits, P.: Transitions from functionalization to fragmentation reactions of laboratory secondary organic

AMTD
8, 3883–3932, 2015

aerosol (SOA) generated from the OH oxidation of alkane precursors., Environ. Sci. Technol., 46, 5430–5437, doi:10.1021/es300274t, 2012.

Lambe, A. T., Cappa, C. D., Massoli, P., Onasch, T. B., Forestieri, S. D., Martin, A. T., Cummings, M. J., Croasdale, D. R., Brune, W. H., Worsnop, D. R., and Davidovits, P.: Relationship between oxidation level and optical properties of secondary organic aerosol., Environ. Sci. Technol., 47, 6349–6357, doi:10.1021/es401043j, 2013.

Lambe, A. T., Chhabra, P. S., Onasch, T. B., Brune, W. H., Hunter, J. F., Kroll, J. H., Cummings, M. J., Brogan, J. F., Parmar, Y., Worsnop, D. R., Kolb, C. E., and Davidovits, P.: Effect of oxidant concentration, exposure time, and seed particles on secondary organic aerosol chemical composition and yield, Atmos. Chem. Phys., 15, 3063–3075, doi:10.5194/acp-15-3063-2015, 2015.

Legrini, O., Oliveros, E., and Braun, A. M.: Photochemical processes for water treatment, Chem. Rev., 93, 671–698, doi:10.1021/cr00018a003, 1993.

Levy II, H.: Normal atmosphere: large radical and formaldehyde concentrations predicted, Science, 173, 141–143, doi:10.1126/science.173.3992.141, 1971.

Li, R., Palm, B. B., Borbon, A., Graus, M., Warneke, C., Ortega, A. M., Day, D. A., Brune, W. H., Jimenez, J. L., and de Gouw, J. A.: Laboratory studies on secondary organic aerosol formation from crude oil vapors, Environ. Sci. Technol., 47, 12566–12574, doi:10.1021/es402265y, 2013.

Li, R., Palm, B. B., Ortega, A. M., Hu, W., Peng, Z., Day, D. A., Knote, C., Brune, W. H., de Gouw, J. A., and Jimenez, J. L.: Modeling the radical chemistry in an Oxidation Flow Reactor (OFR): radical formation and recycling, sensitivities, and OH exposure calibration equation, J. Phys. Chem. A, in press, doi:10.1021/jp509534k, 2015.

Liu, P. F., Abdelmalki, N., Hung, H.-M., Wang, Y., Brune, W. H., and Martin, S. T.: Ultraviolet and visible complex refractive indices of secondary organic material produced by photooxidation of the aromatic compounds toluene and *m*-xylene, Atmos. Chem. Phys., 15, 1435–1446, doi:10.5194/acp-15-1435-2015, 2015.

Ma, X. and Xia, Y.: Pinpointing double bonds in lipids by Paternò-Büchi reactions and mass spectrometry, Angew. Chem. Int. Edit., 53, 2592–2596, doi:10.1002/anie.201310699, 2014.

Mao, J., Ren, X., Brune, W. H., Olson, J. R., Crawford, J. H., Fried, A., Huey, L. G., Cohen, R. C., Heikes, B., Singh, H. B., Blake, D. R., Sachse, G. W., Diskin, G. S., Hall, S. R., and Shetter, R. E.: Airborne measurement of OH reactivity during INTEX-B, Atmos. Chem. Phys., 9, 163–173, doi:10.5194/acp-9-163-2009, 2009.

AMTD
8, 3883–3932, 2015

Massoli, P., Lambe, A. T., Ahern, A. T., Williams, L. R., Ehn, M., Mikkilä, J., Canagaratna, M. R., Brune, W. H., Onasch, T. B., Jayne, J. T., Petäjä, T., Kulmala, M., Laaksonen, A., Kolb, C. E., Davidovits, P., and Worsnop, D. R.: Relationship between aerosol oxidation level and hygroscopic properties of laboratory generated secondary organic aerosol (SOA) particles, Geophys. Res. Lett., 37, L24801, doi:10.1029/2010GL045258, 2010.

Nehr, S., Bohn, B., Dorn, H.-P., Fuchs, H., Häseler, R., Hofzumahaus, A., Li, X., Rohrer, F., Tillmann, R., and Wahner, A.: Atmospheric photochemistry of aromatic hydrocarbons: OH budgets during SAPHIR chamber experiments, Atmos. Chem. Phys., 14, 6941–6952, doi:10.5194/acp-14-6941-2014, 2014.

Ono, R., Nakagawa, Y., Tokumitsu, Y., Matsumoto, H., and Oda, T.: Effect of humidity on the production of ozone and other radicals by low-pressure mercury lamps, J. Photochem. Photobiol. A Chem., 274, 13–19, doi:10.1016/j.jphotochem.2013.09.012, 2014.

Ortega, A. M., Day, D. A., Cubison, M. J., Brune, W. H., Bon, D., de Gouw, J. A., and Jimenez, J. L.: Secondary organic aerosol formation and primary organic aerosol oxidation from biomass-burning smoke in a flow reactor during FLAME-3, Atmos. Chem. Phys., 13, 11551–11571, doi:10.5194/acp-13-11551-2013, 2013.

Palm, B. B., Campuzano-Jost, P., Ortega, A. M., Day, D. A., Karl, T., Kaser, L., Jud, W., Hansel, A., Fry, J. L., Brown, S. S., Zarzana, K. J., Dube, W. P., Wagner, N. L., Draper, D. C., Hunter, J. F., Kroll, J. H., Brune, W. H., and Jimenez, J. L.: Real-time organic aerosol formation and oxidative aging using a flow reactor in a pine forest, in preparation, 2015.

Peng, Z., Dobrijevic, M., Hébrard, E., Carrasco, N., and Pernot, P.: Photochemical modeling of Titan atmosphere at the "10 percent uncertainty horizon," Faraday Discuss., 147, 137, doi:10.1039/c003366a, 2010.

Peng, Z., Cailliez, F., Dobrijevic, M., and Pernot, P.: Null Variance Altitudes for the photolysis rate constants of species with barometric distribution: illustration on Titan upper atmosphere modeling, Icarus, 218, 950–955, doi:10.1016/j.icarus.2012.02.006, 2012.

Peng, Z., Carrasco, N., and Pernot, P.: Modeling of synchrotron-based laboratory simulations of Titan's ionospheric photochemistry, GeoResJ, 1–2, 33–53, doi:10.1016/j.grj.2014.03.002, 2014.

Platt, S. M., El Haddad, I., Zardini, A. A., Clairotte, M., Astorga, C., Wolf, R., Slowik, J. G., Temime-Roussel, B., Marchand, N., Ježek, I., Drinovec, L., Močnik, G., Möhler, O., Richter, R., Barmet, P., Bianchi, F., Baltensperger, U., and Prévôt, A. S. H.: Secondary or-

AMTD
8, 3883–3932, 2015

ganic aerosol formation from gasoline vehicle emissions in a new mobile environmental reaction chamber, Atmos. Chem. Phys., 13, 9141–9158, doi:10.5194/acp-13-9141-2013, 2013.
Presto, A. A., Huff Hartz, K. E., and Donahue, N. M.: Secondary organic aerosol production from terpene ozonolysis. 1. Effect of UV radiation, Environ. Sci. Technol., 39, 7036–7045, doi:10.1021/es050174m, 2005.
Saltelli, A., Ratto, M., Tarantola, S., and Campolongo, F.: Sensitivity analysis for chemical models., Chem. Rev., 105, 2811–2828, doi:10.1021/cr040659d, 2005.
Sander, S. P., Friedl, R. R., Barker, J. R., Golden, D. M., Kurylo, M. J., Sciences, G. E., Wine, P. H., Abbatt, J. P. D., Burkholder, J. B., Kolb, C. E., Moortgat, G. K., Huie, R. E., and Orkin, V. L.: Chemical Kinetics and Photochemical Data for Use in Atmospheric Studies Evaluation Number 17, available at: http://jpldataeval.jpl.nasa.gov/pdf/JPL10-6Final15June2011.pdf (last access: April 2015), 2011.
Saukko, E., Lambe, A. T., Massoli, P., Koop, T., Wright, J. P., Croasdale, D. R., Pedernera, D. A., Onasch, T. B., Laaksonen, A., Davidovits, P., Worsnop, D. R., and Virtanen, A.: Humidity-dependent phase state of SOA particles from biogenic and anthropogenic precursors, Atmos. Chem. Phys., 12, 7517–7529, doi:10.5194/acp-12-7517-2012, 2012.
Seakins, P. W.: A brief review of the use of environmental chambers for gas phase studies of kinetics, chemical mechanisms and characterisation of field instruments, EPJ Web Conf., 9, 143–163, doi:10.1051/epjconf/201009012, 2010.
Stone, D., Whalley, L. K., and Heard, D. E.: Tropospheric OH and HO_2 radicals: field measurements and model comparisons, Chem. Soc. Rev., 41, 6348–6404, doi:10.1039/c2cs35140d, 2012.
Tkacik, D. S., Lambe, A. T., Jathar, S., Li, X., Presto, A. A., Zhao, Y., Blake, D., Meinardi, S., Jayne, J. T., Croteau, P. L., and Robinson, A. L.: Secondary organic aerosol formation from in-use motor vehicle emissions using a potential aerosol mass reactor, Environ. Sci. Technol., 48, 11235–11242, doi:10.1021/es502239v, 2014.
Volkamer, R., Jimenez, J. L., San Martini, F., Dzepina, K., Zhang, Q., Salcedo, D., Molina, L. T., Worsnop, D. R., and Molina, M. J.: Secondary organic aerosol formation from anthropogenic air pollution: rapid and higher than expected, Geophys. Res. Lett., 33, L17811, doi:10.1029/2006GL026899, 2006.
Wakelam, V., Smith, I. W. M., Herbst, E., Troe, J., Geppert, W., Linnartz, H., Öberg, K., Roueff, E., Agúndez, M., Pernot, P., Cuppen, H. M., Loison, J. C., and Talbi, D.: Reaction

AMTD
8, 3883–3932, 2015

networks for interstellar chemical modelling: improvements and challenges, Space Sci. Rev., 156, 13–72, doi:10.1007/s11214-010-9712-5, 2010.

Wang, B., Lambe, A. T., Massoli, P., Onasch, T. B., Davidovits, P., Worsnop, D. R., and Knopf, D. A.: The deposition ice nucleation and immersion freezing potential of amorphous secondary organic aerosol: pathways for ice and mixed-phase cloud formation, J. Geophys. Res., 117, D16209, doi:10.1029/2012JD018063, 2012.

Wang, J., Doussin, J. F., Perrier, S., Perraudin, E., Katrib, Y., Pangui, E., and Picquet-Varrault, B.: Design of a new multi-phase experimental simulation chamber for atmospheric photosmog, aerosol and cloud chemistry research, Atmos. Meas. Tech., 4, 2465–2494, doi:10.5194/amt-4-2465-2011, 2011.

Witte, K. J., Burkhard, P., and Lüthi, H. R.: Low-pressure mercury lamp pumped atomic iodine laser of high efficiency, Opt. Commun., 28, 202–206, doi:10.1016/0030-4018(79)90268-2, 1979.

Ye, J., Shang, J., Li, Q., Xu, W., Liu, J., Feng, X., and Zhu, T.: The use of vacuum ultraviolet irradiation to oxidize SO_2 and NO_x for simultaneous desulfurization and denitrification, J. Hazard. Mater., 271, 89–97, doi:10.1016/j.jhazmat.2014.02.011, 2014.

AMTD
8, 3883–3932, 2015

Table 1. Code of the labels of typical cases. A case label is composed of three characters denoting the water mixing ratio, the photon flux, and the external OH reactivity, respectively.

	Water mixing ratio	Photon flux	External OH reactivity
Options	L = low (0.07 %)	L = low (10^{11} photons cm^{-2} s^{-1} at 185 nm; 4.2×10^{13} photons cm^{-2} s^{-1} at 254 nm)	0
	M = medium (1 %)	M = medium (10^{13} photons cm^{-2} s^{-1} at 185 nm; 1.4×10^{15} photons cm^{-2} s^{-1} at 254 nm)	L = low (10 s^{-1})
	H = high (2.3 %)	H = high (10^{14} photons cm^{-2} s^{-1} at 185 nm; 8.5×10^{15} photons cm^{-2} s^{-1} at 254 nm)	H = high (100 s^{-1})
	* = the whole range	* = the whole range	V = very high (1000 s^{-1})
Examples	LH0:	low water mixing ratio, high photon flux, no external OH reactivity	
	M*H:	medium water mixing ratio, whole explored range of photon flux, high external OH reactivity	

AMTD
8, 3883–3932, 2015

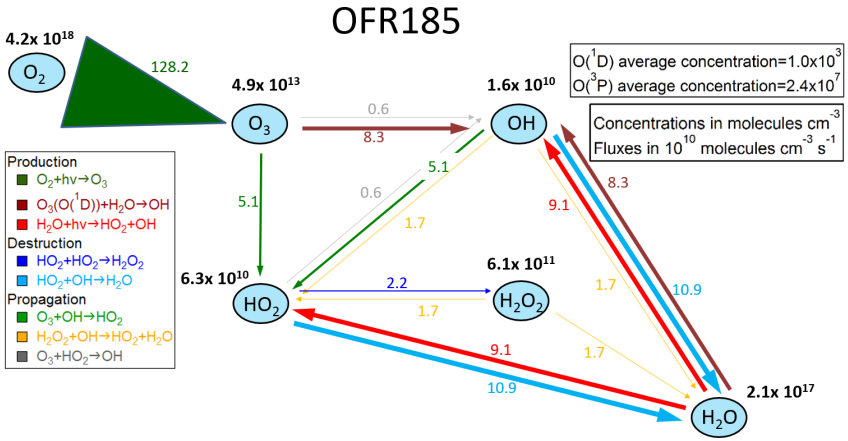

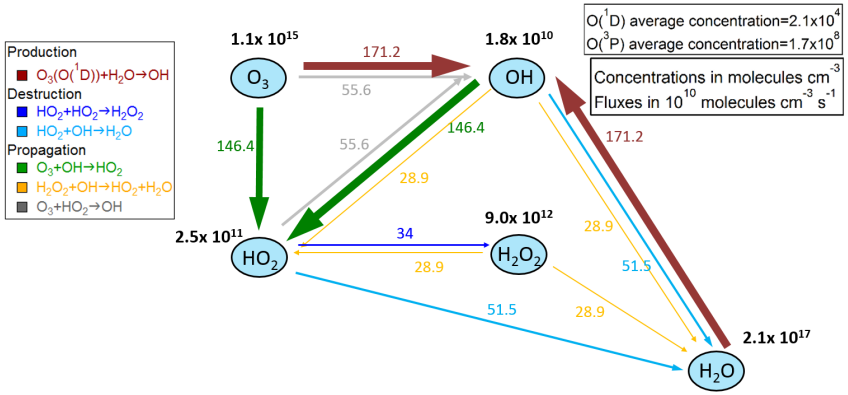

AMTD
8, 3883–3932, 2015

HO$_x$ radical chemistry in oxidation flow reactors

Z. Peng et al.

Figure 1. Schematics of main species and major reaction pathways for a case with medium H_2O and UV, and zero OHR_{ext}, for both OFR185 and OFR254-70. Species average concentrations (in molecules cm^{-3}) are shown in black beside species names. Arrows denote directions of the conversions. Average reaction fluxes (in units of 10^{10} molecules $cm^{-3}\,s^{-1}$) are calculated according to the production rate, and shown on or beside the corresponding arrows and in the same color. Within each schematic, the thickness of the arrows is a measure of their corresponding species flux. Multiple arrows in the same color and pointing to the same species should be counted only once for reaction flux on a species. Note that all values in these schematics are average ones over the residence time, and not obtained from steady state. In the legend, reactions are classified as production, destruction, and propagation of HO_x. Since the reactions involving O and H atoms are very fast, they are not shown explicitly.

AMTD
8, 3883–3932, 2015

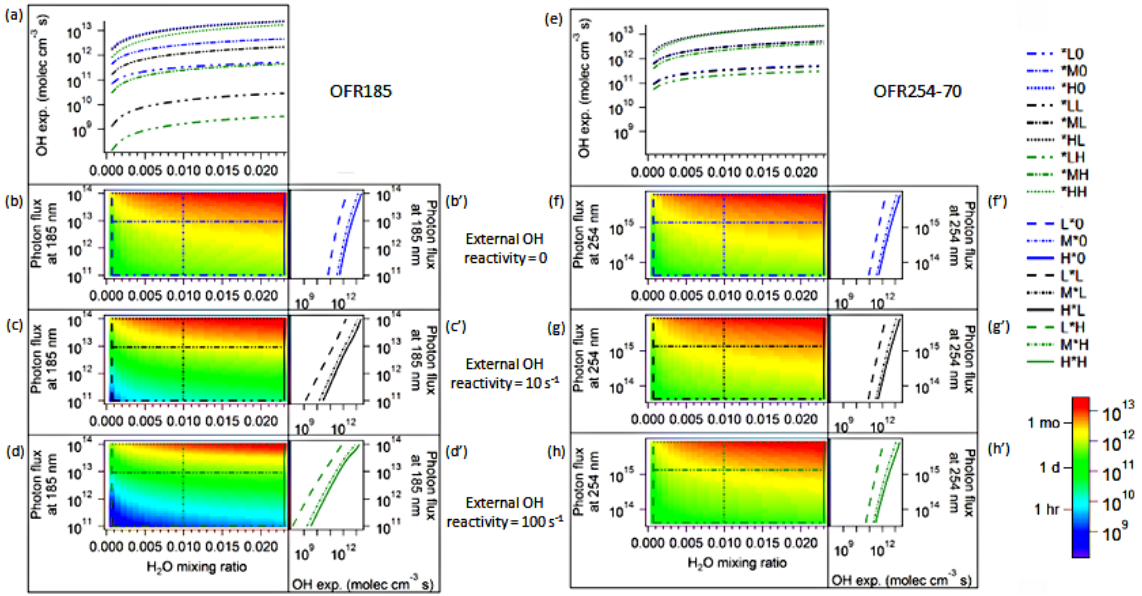

Figure 2. Dependence of OH exposures (in molecules cm^{-3} s) in OFR185 and OFR254-70 on H_2O and UV, for OHR_{ext} of **(b, f)** 0, **(c, g)** 10 and **(d, h)** 100 s^{-1}. **(a, e)** and **(b′–h′)** are the line plots of OH exposures of several typical cases. These cases are denoted in the image plots **(b–h)** by horizontal or vertical lines of the same color and pattern as in the line plots. In detail, the cut lines are in blue, black, and dark green in the plots for the cases of 0, low, and high external OH reactivity, respectively. Horizontal sparse-dash-dot-dot, dash-dot-dot, and dotted lines mark low, medium, and high water mixing ratios, respectively (first legend box). Vertical dashed, dash-dot, and solid lines mark low, medium, and high photon fluxes, respectively (second legend box). Refer to Table 1 for more details on case labels. The color scale corresponds to all image plots. Equivalent ambient exposure time (based on average ambient OH concentration of 1.5×10^6 molecules cm^{-3}, Mao et al., 2009) is also indicated in the color scale.

AMTD
8, 3883–3932, 2015

HO$_x$ radical chemistry in oxidation flow reactors

Z. Peng et al.

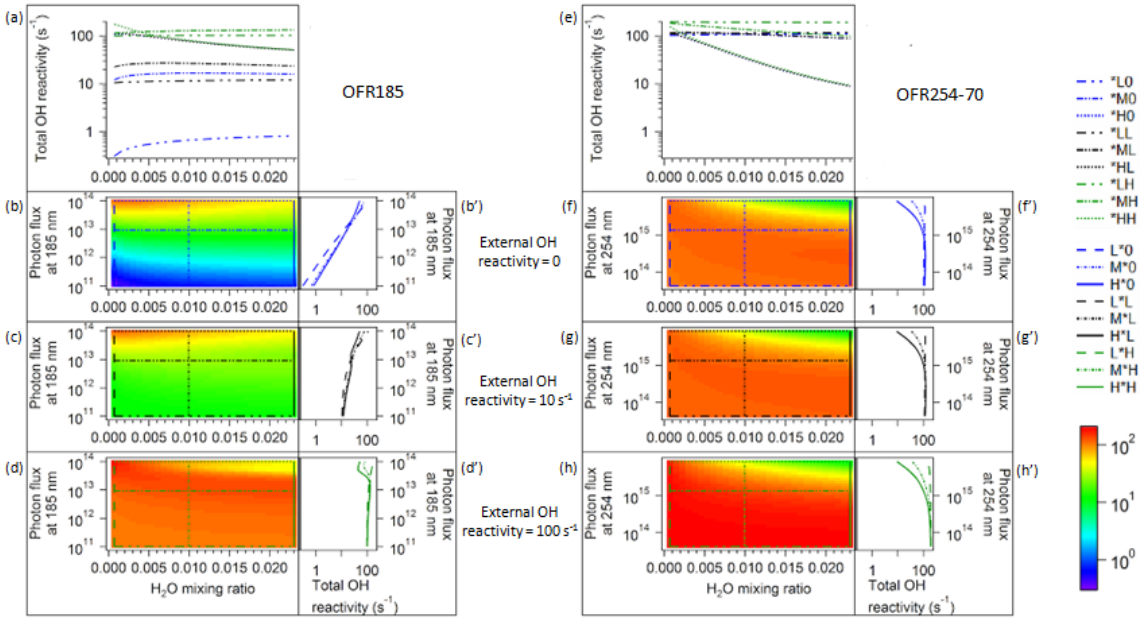

Figure 3. O_3 exposure (in molecules cm^{-3} s) vs. the same parameters and in the same format as Fig. 2. Equivalent ambient exposure time (based on average ambient O_3 mixing ratio of 34 ppb, Environment Canada, 2014) is also indicated in the color scale.

AMTD
8, 3883–3932, 2015

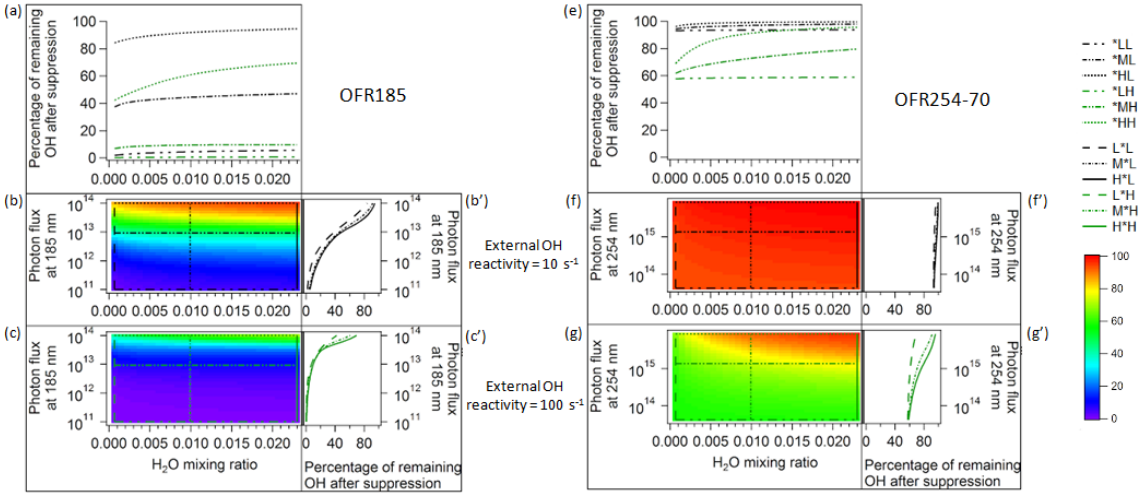

Figure 4. Percentage of remaining OH after suppression vs. the same parameters and in the same format Fig. 2, but without the case of no external OH reactivity, which is the reference case.

AMTD
8, 3883–3932, 2015

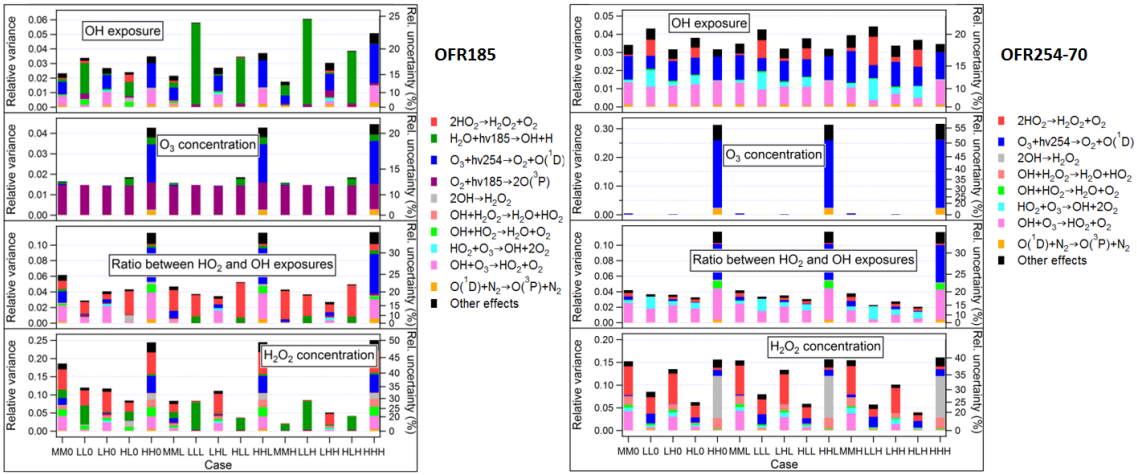

Figure 5. Relative variances (left axes)/uncertainties (right axes) of the outputs (i.e., OH exposure, O_3 concentration, ratios between HO_2 and OH exposure, and H_2O_2 concentration) of Monte Carlo uncertainty propagation, and relative contributions of key reactions to these relative variances in typical cases in OFR185 and OFR254-70. Relative variances are shown in linear scales (left axis), while corresponding relative uncertainties, equal to relative variances' square roots, are indicated by the non-linear right axis. Only the reactions with a contribution of no less than 0.04 to at least 1 relative variance are shown.

AMTD
8, 3883–3932, 2015

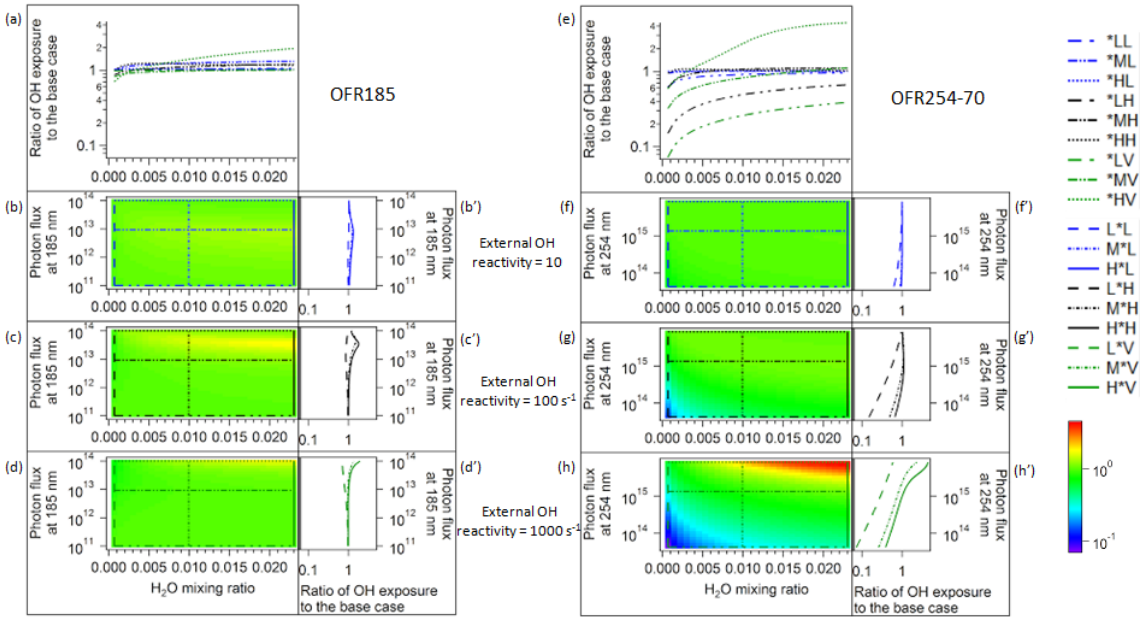

Figure 6. Percentage of OH exposure in the case of HO_x-destructive external OH reactivity (OHR_{ext}) relative to that in the base case (Fig. 2) vs. the same parameters and in the same format as Fig. 2, but for the cases of low ($10\,s^{-1}$), high ($100\,s^{-1}$), and very high ($1000\,s^{-1}$) external OH reactivity.

AMTD
8, 3883–3932, 2015

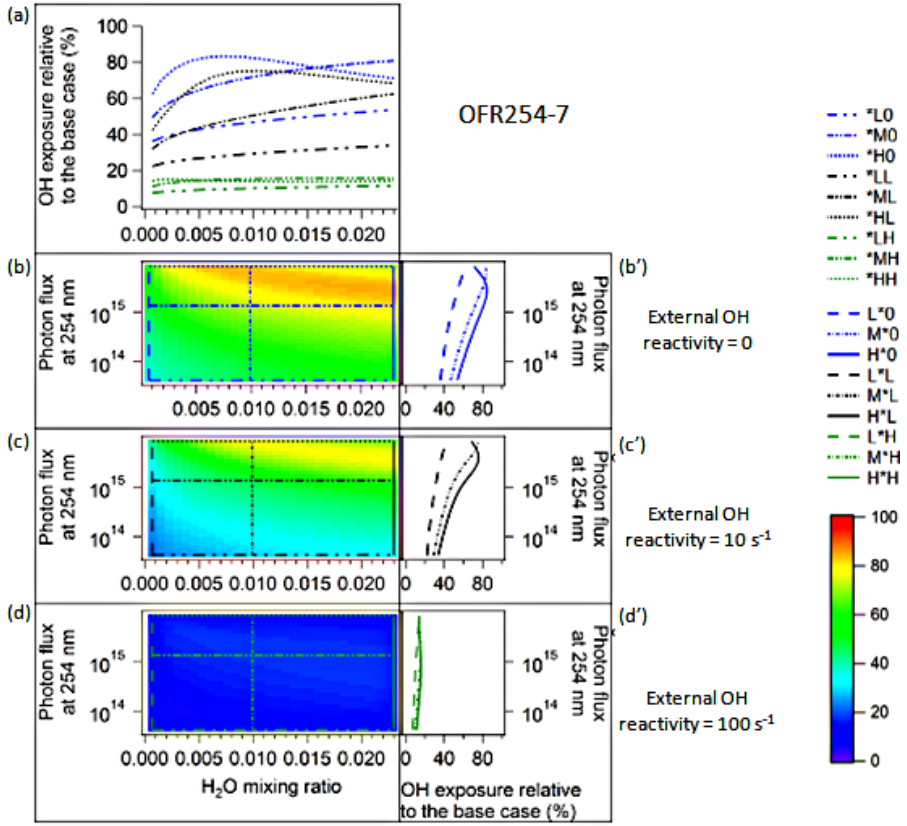

Figure 7. Percentage of OH exposure in OFR254-7 to the base case (OFR254-70) vs. the same parameters and in the same format as Fig. 2e–h, f′–h′.

AMTD
8, 3883–3932, 2015

HO$_x$ radical chemistry in oxidation flow reactors

Z. Peng et al.

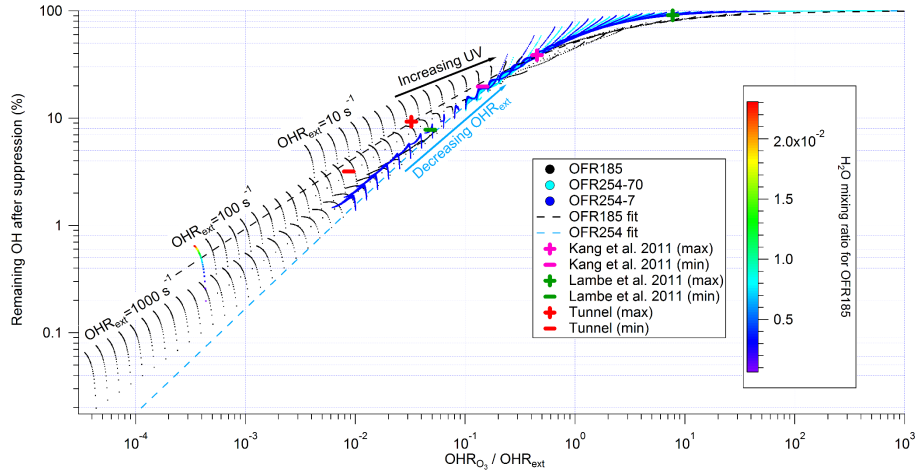

Figure 8. Percentage of remaining OH after suppression in OFR185 (black dot), OFR254-70 (cyan dot), and OFR254-7 (blue dot) vs. the ratio of OH reactivity from O_3 to external OH reactivity (OHR_{ext}). The three series of OFR185 data points corresponding to OHR_{ext} = 10, 100, and 1000 s^{-1} are respectively labeled. A strip of OFR185 data points are colored by H_2O mixing ratio. The fit curves for OFR185 (black dash) and OFR254 (light blue dash) are shown. The estimated ranges for laboratory experiments (Kang et al., 2011; Lambe et al., 2011b) (pink and green markers, respectively) and a source study in an urban tunnel (Tkacik et al., 2014) (red marker) are also shown for comparison. These ranges are estimated by the present model according to the conditions reported in these studies.

AMTD
8, 3883–3932, 2015

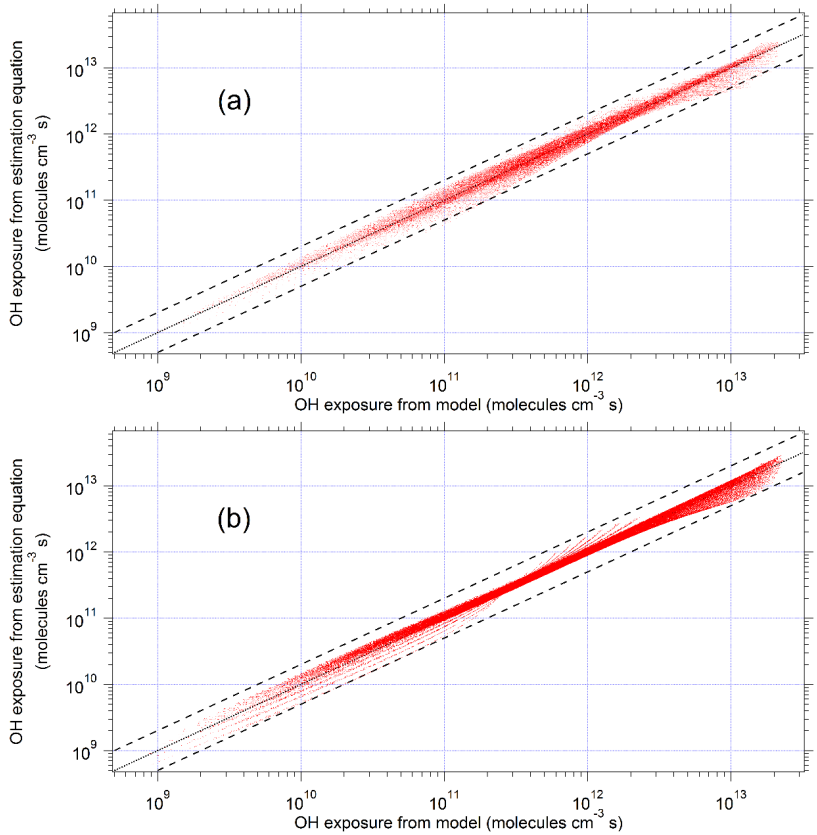

Figure 9. Comparison of OH exposure (OH_{exp}) estimated from the estimation equations, i.e., **(a)** Eq. (5) and **(b)** Eq. (6), vs. the model results. 1 : 1, 1 : 2, and 2 : 1 lines are also shown to facilitate the comparison.

AMTD
8, 3883–3932, 2015